J. Fluid Mech. (2000), *vol.* 423, *pp.* 227–261. Printed in the United Kingdom

An experimental study of a boundary layer that is maintained on the verge of separation

By K. ELSBERRY†, J. LOEFFLER‡, M. D. ZHOU AND I. WYGNANSKI¶

Department of Aerospace and Mechanical Engineering, University of Arizona, Tucson, AZ, 85721, USA

(Received 27 April 1999 and in revised form 28 April 2000)

A boundary layer maintained as close as possible to separation over an extended distance was produced, in accordance with the concept of Stratford. The resulting layer was two-dimensional in the mean, had nearly a constant shape factor of 2.5 and approximately linear streamwise growth of its integral length scales. The flow exhibited a definite non-equilibrium character, indicated by the different scales required for collapse of the mean velocity and turbulence intensity profiles. It was also very sensitive to the thickness of the upstream boundary layer. External excitation was imposed for diagnostic purposes and as a tool for delaying separation. The oscillatory momentum level of $c_\mu \approx 0.1\%$ was tested for its ability to increase the skin friction c_f at the prescribed geometry. Various frequencies, corresponding to the Strouhal number $0.008 < f\theta_0/U_{ref} < 0.064$, were used for the free stream reference velocity of $U_{ref} = 15\,\mathrm{m\,s^{-1}}$ and for two different inflow conditions. Notable increase (close to 60%) in c_f was observed at higher frequencies that did not undergo maximum amplification. The increase in c_f was accompanied by a reduction in the boundary layer thickness and in the shape factor H. The latter decreased in one case from 2.5 to 2.1. The overall turbulence level in the boundary layer decreased due to the addition of plane external perturbations.

1. Introduction

The behaviour of boundary layers subjected to severe adverse pressure gradient is of great technological interest. Adverse pressure gradients occur whenever a solid surface turns away from the mean flow direction, as it does near the trailing edges of airfoils or at the termination of streamlined bodies such as submarines or ships. Adverse pressure gradients also occur in diverging channels, exemplified in aeronautical applications by inlets to engines. It is generally desirable to minimize the distance over which the deceleration takes place but this desire is tempered by the requirement to avoid separation and flow reversal. For example, airfoil designers would like to minimize the length of the pressure recovery section in order to maximize the fraction of the airfoil chord that can sustain natural laminar flow. For streamlined bodies, a rapid truncation provides more useable volume per unit surface area and greater structural efficiency. For diffusers, a reduction in duct length reduces weight and lost volume.

Separation results in large total pressure losses, buffet, loss of lift and loss of control.

† Present Address: Raytheon Missile Systems Company, Tucson, AZ 85734-1337, USA.
‡ Present Address: Eurocopter, Germany.
¶ Also Lazarus Professor of Aerodynamics, Faculty of Engineering, University of Tel-Aviv.

It has to be avoided but so does a conservative, large and overweight design. These competing priorities have led several investigators to examine the largest adverse pressure gradient that can be sustained without causing separation. Stratford (1959*a*) proposed that a turbulent boundary layer providing a maximum rate of pressure recovery has to have a zero wall stress over its entire length. He began by conceptually dividing the velocity profile into two parts: an outer part, that merely loses dynamic head in direct proportion to the increase in static pressure, and an inner part that maintains an equilibrium between the transverse gradient of the shear stress and the stream-wise pressure gradient. The mixing length hypothesis was invoked as well as some assumptions about the general shape of the velocity profile in order to derive an equation for the pressure recovery that corresponds to an imminent, continuous separation. In Stratford (1959*b*) this analysis was backed by an experiment in which a stable turbulent boundary layer with a 'near zero skin friction' was generated. Stratford's experiment was limited by the available instrumentation (Pitot tubes) and was marred by a lack of two-dimensionality. The concept, however, lead the way to a novel design of airfoils for high lift (Liebeck 1973) because it provides the maximum pressure rise that a boundary layer can sustain without separation, in the shortest possible distance.

Spangenberg, Rowland & Mease (1967) attempted to produce such a flow on a flat surface by using a vented wind-tunnel wall and an adjustable 'end-gate' at the end of their test section. Their results cast doubt on some of the theoretical claims of Stratford, particularly with regard to the existence of a region of linear variation of the dynamic head with increasing distance from the wall. Furthermore, they produced two very different sets of data with approximately the same pressure distribution suggesting that, in addition to factors usually considered, the inflow conditions influence the behaviour of the boundary layer near separation. Notably, the case with lower skin friction exhibited greater loss of mean kinetic energy.

Dengel & Fernholz (1990, hereafter referred to as DF) examined the sensitivity of a turbulent boundary layer near separation to small differences in pressure gradient by using the same technique as Spangenberg *et al.* (1967). Their measurements were carried out on a large cylinder thus reducing the difficulties associated with two-dimensionality. One of their tests generated a region where the boundary layer possessed a zero averaged skin friction. In this region, the flow reversed its direction next to the surface roughly 50% of the total time. Another experiment of note is by Skare & Krogstad (1994, hereafter referred to as SK) who concentrated on the equilibrium aspects of a boundary layer that is subjected to a severe adverse pressure gradient but does not approach separation. Their measured skin friction coefficient, c_f, in the region of interest was 5.7×10^{-4} and the shape factor of the boundary layer $H = 2$. It is worth noting that only Stratford made his measurements on the boundary layer evolving over the curved surface. There are many other experiments focusing on the process of separation (e.g. Perry & Schofield 1973; Simpson 1989; Patrick 1987) but they will not be discussed in the present context. The purpose of the research to be described is to consider the boundary layer that is maintained on the brink of separation without actually detaching fully from the surface over a significant distance or time. The measurements were conducted on a curved surface in parallel with numerical experiments of H. Fasel and closure models of C. Speziale in the hope that the data be used to validate models needed to simulate flows in large adverse pressure gradients.

All the experiments involving active control of separation were carried out on conventionally designed airfoils, wings or diffusers. Separation occurred naturally at

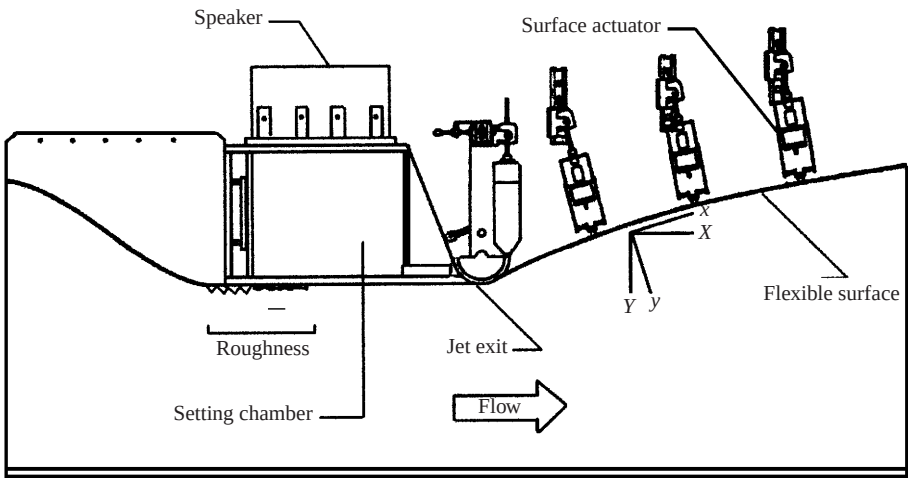

FIGURE 1. Experimental facility.

off-design conditions due to excessive incidence, flap deflections, too low Reynolds numbers or too high Mach Numbers. Active flow control (AFC, Wygnanski 1997) enabled the flow remain attached beyond the conventional design limits of the prescribed configuration and thus improve the performance.

A historical perspective on many aspects of flow control is documented in the books edited by Lachmann (1961) and written by Chang (1976). More recent surveys on passive and active flow management methods were carried out by Gad el Hak & Bushnell (1991) and by Fernholz (1993). Both articles discuss active and passive management techniques of turbulent shear flows and their respective merits. All, however, take the design of a wing, an airfoil or a streamlined body, that was based on a steady flow assumption as given. They reveal, therefore, that active flow control is only a concept but not a technology because it does not provide an engineer with integrated design criteria that optimize the shape of a streamlined body with built-in actuators for prescribed actuation levels and frequencies.

The present experiment also describes the effects of periodic excitation on the boundary layer parameters such as skin friction and shape factor under prescribed boundary and inflow conditions. It is but a first step in the process of determining the optimum shape of the surface that is capable of maintaining a boundary layer on the brink of separation for a prescribed level of periodic excitation. In the next step the original parameters of the flow will be restored (while maintaining the external actuation) by changing and adjusting the geometry of the surface.

2. Apparatus and experimental conditions

The experimental facility consists of a two-dimensional contraction, a constant-area throat, and a two-dimensional variable-geometry expansion inserted into the 0.61 m by 0.92 m test section of a closed-loop, low speed wind tunnel at the University of Arizona (figure 1). The expansion is constructed of 3.2 mm thick Lexan and is supported by six electric actuators. The actuators are driven by step motors via lead-screws. This allows precise computer controlled motion of the surface. The gimbals allow the surface geometry to be varied over very wide limits in both the streamwise and cross-stream directions.

The transition between the throat and the test surface is accomplished by means of a 15.24 cm diameter cylinder. The cylinder is also provided with an electric actuator that enables the initial slope of the test surface to be changed. This cylinder causes the form of the adverse pressure gradient to deviate somewhat from the ideal Stratford pressure distribution, which is discontinuous at the initiation of the adverse pressure gradient. The present geometry is, however, more representative of likely applications. The shape of the flexible surface is approximately described by the following:

$$\textit{case A} \qquad Y = 0.39696 + 0.38091X - 8.925 \times 10^{-5}X^2 - 6.8277 \times 10^{-6}X^3,$$

where X and Y are defined in this context as being parallel and normal to the floor of the tunnel, respectively, and are measured from the beginning of the flexible surface. For all measurements reported here the velocity in the tunnel was set at $U_{ref} = 15\,\mathrm{m\,s^{-1}}$, measured by a Pitot tube in the constant-area throat section of the test apparatus (figure 1) and sufficiently far upstream of the divergence. Since the flow accelerated near the initiation of the divergence, the inflow conditions were specified at a location at which the free stream velocity (in the absence of excitation) reached its maximum value, U_0 (see § 4). Streamline coordinates (x, y) are used to analyse the data; thus the initial momentum thickness of the boundary layer

$$\theta_0 = \int \frac{U}{U_0}\left(1 - \frac{U}{U_0}\right) \mathrm{d}y$$

measured at the x-location where the free-stream velocity was U_0, was 2.3 mm. Many distances in the direction of streaming are referred to the virtual origin of the flow, x_0, where the extrapolated curve of the local momentum thickness, θ, would have vanished.

The significance of changing the inflow conditions on the evolution of the ensuing boundary layer was also assessed in this experiment. Roughness strips glued to the narrow, straight surface upstream of the divergent section (figure 1) changed θ_0 from 2.3 mm to 4.5 mm. Thereafter the shape of the divergent surface had to be adjusted slightly to maintain the flow on the verge of continuous separation. The shape of the new configuration is

$$\textit{case B} \qquad Y = 0.35189 + 0.40782X - 1.33 \times 10^{-3}X^2 - 1.03879 \times 10^{-7}X^3.$$

All the data required for making the balance of turbulent energy were for case A. The data were generally acquired at a frequency of 2 KHz but for assessing the dissipation the sampling rate this was increased to 20 KHz.

Preliminary work indicated that sidewall interference was likely to pose a significant difficulty because the interaction of the boundary layer on the sidewalls with the boundary layer on the test surface causes premature separation. This was initially avoided by adding fences to both sides of the test surface, thereby initiating a fresh boundary layer at the leading edge of the fence. Although this provided a solution to the problem, it did not ensure success at various inflow conditions. Therefore a narrow suction slot was cut into each sidewall, at the start of the expansion section and was connected to an independent low pressure source. This arrangement allowed the sidewall boundary layers to be removed, maintaining two-dimensional flow even at the most distant measuring location downstream. This was checked in several ways; by using multiple static pressure taps distributed along the span, by measurements of W and measurements of $\overline{u'w'}$, and by integration of the two-dimensional boundary layer equations to obtain the value of $\overline{u'v'}$ that agrees with direct measurement. The mean value of the spanwise component of velocity did not exceed 1% of the

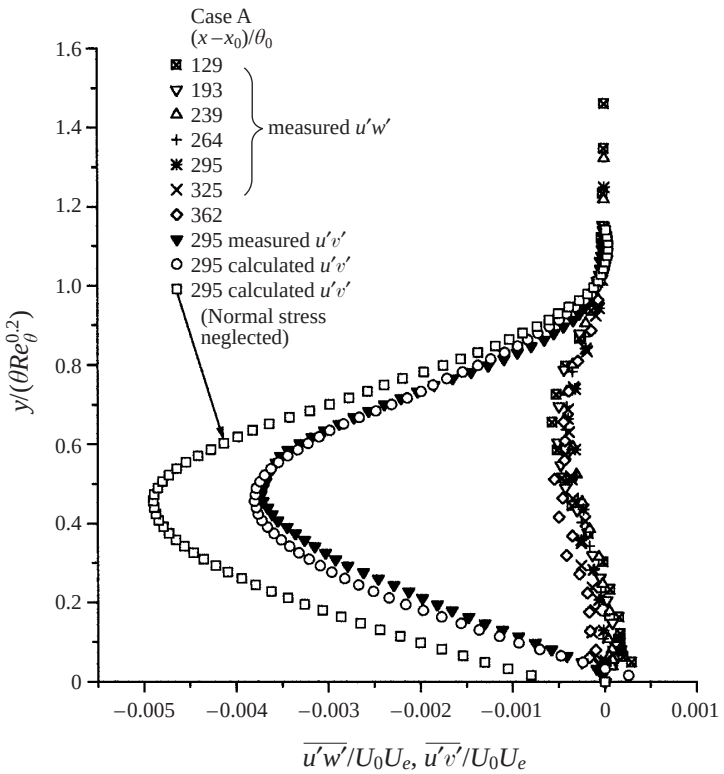

FIGURE 2. Spanwise and longitudinal Reynolds stresses for different downstream locations.

streamwise mean velocity at any measured location. Given the uncertainty in the probe angle with respect to the mean flow it was concluded that the spanwise mean velocity component was essentially zero. The value of the spanwise Reynolds stress, $\overline{u'w'}$, is presented in figure 2. The peak of this quantity is more than one order of magnitude smaller than the peak of the corresponding longitudinal quantity in spite of the presence of streamwise vortices arising from the concave curvature of the surface. Finally, the Reynolds stress calculated by integrating the two-dimensional momentum equation (5.2), using the measured streamwise component of velocity U, the continuity equation $V(y) = -\int_0^y (\partial U/\partial x)\mathrm{d}y$, and the measured normal stresses $(u'^2 - v'^2)$, agrees very well with the directly measured Reynolds stress (figure 2). All these tests confirm the two-dimensionality of the flow and prove the reliability of the measurements.

The pressure distribution was initially obtained by increasing the divergence of the surface until any further increase led to total separation. At each stage of increased divergence it was necessary to determine the asymptotic value of the sidewall suction. This was done by placing a hot-wire probe at the most downstream location used in the experiment and varying the suction until further increases did not alter the observed velocity. Any attempt to increase the rate of pressure recovery beyond this value was unsuccessful regardless of the level of suction from the sidewalls. Tufts glued to the surface of the ramp indicated that periodic back-flow was present.

The high turbulence intensity and the sensitivity of the flow to external disturbances demanded a special support for the probe holders used in the study. The support must have a high stiffness to mass ratio, minimal blockage, and the ability to vary the

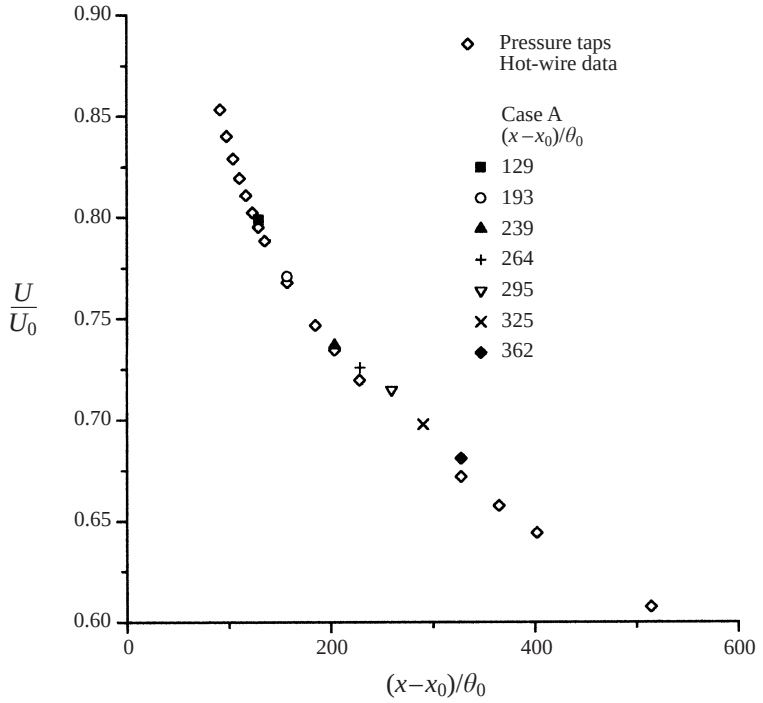

FIGURE 3. Deceleration of the flow for the thin inflow condition (case A).

probe angle (to calibrate x-wire probes and to allow for wall curvature). The support is of an open, girder construction originally proposed by D. W. Bechert (private communication) and it is essentially immune to aeroelastic vibrations.

Previous experimental observations (Simpson 1989) suggested that prior to complete separation from the surface, there is a region where the mean flow still proceeds downstream but in which the turbulent fluctuations produce periods of reversed flow. The fraction of time that the flow proceeds upstream in a region close to the wall, γ, has been used to define the mean separation location. A common formulation is that incipient detachment has occurred when the probabilities of forward and reverse flow are equal (Simpson 1989). This definition was deemed most appropriate when attempting to reproduce a boundary layer matching the Stratford concept. However, it proved to be unworkable because the flow is sensitive to random perturbations in the laboratory and could detach itself suddenly without apparent cause. We had therefore to content ourselves with a flow that was stable but was close enough to separation. The proximity of the flow to separation was therefore determined from the mean velocity profiles plotted in wall coordinates.

The deceleration of the flow for the thin inflow condition (case A) is shown in figure 3. The close agreement between the velocity inferred from the pressure distribution and the external velocity measured with a hot wire indicates that the boundary layer approximation can be applied.

Harmonic oscillations were introduced to the flow field through a thin slot close to the initiation of the adverse pressure gradient. Although these oscillations originated from a loudspeaker located on top of the settling chamber, they emerged as vortical

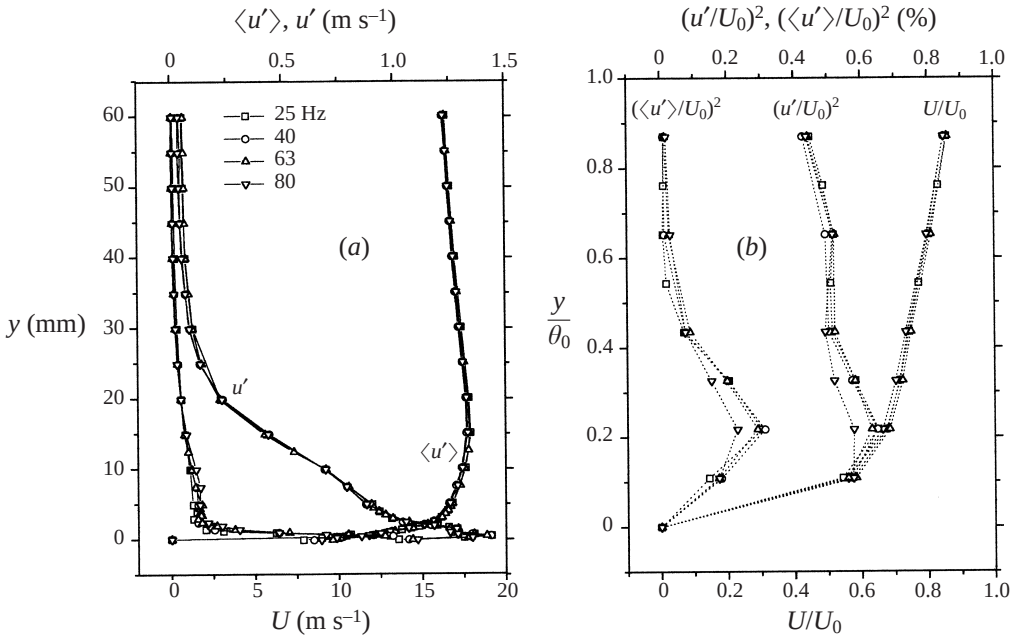

FIGURE 4. The effect of external excitation on the inflow conditions.

perturbations in the flow. All efforts were made to seal the settling chamber and provide two-dimensional perturbations with zero net mass flux.

The inflow conditions for all forcing frequencies are shown in figure 4. For the determination of the forcing level, the distribution of the phase-locked and ensemble-averaged r.m.s. value of the streamwise velocity component was integrated with respect to the normal coordinate. The integral value was then normalized by the momentum deficit at this location

$$c_\mu = \frac{\int_0^\infty \overline{u'^2}\,\mathrm{d}y}{U_0^2\theta_0}. \tag{2.1}$$

A value of $c_\mu \approx 0.1\%$ was achieved for all forcing frequencies regardless of the differences in the detailed distribution of the phased-locked amplitudes near the slot (figure 4*b*). The value of θ_0 near the slot was obtained from extrapolation of the momentum thickness, measured while the flow was not forced, to the location at which the free-stream velocity attained its maximum value, U_0 (this gave $\theta_0 = 2.3$ mm for case A and 4.5 mm for case B).

3. Instrumentation and data reliability

The primary instrument used for the study was the constant-temperature hot-wire anemometer (HW). Single, normal wires and x-wire arrays were used and the data were sampled at 2 KHz except for dissipation measurements where the sampling rate was increased to 20 KHz. This instrument remains the best choice when a statistical description of the flow is required, in spite of the availability of a laser Doppler velocimeter (LDV) and a particle image velocimeter (PIV). The overall reliability of the hot-wire data was demonstrated in figure 2 where balance of the momentum

equation provided a good comparison between the measured and the calculated Reynolds stress. However, the instantaneous velocity vector can deviate significantly from the mean flow direction close to the surface. Special care was therefore taken with the calibration of the x-probes that measured the V component of velocity. In particular, it was desirable to extend the calibration over the full effective range of a 45° x-wire sensor (i.e. to $\pm 40°$). In order to obtain acceptable accuracy a look-up table approach, derived from Leupetow, Bruer & Haritonidis (1988) was adopted for calibrating the x-wire. This technique involves the use of successive polynomial fits to the raw calibration data in order to characterize the U and V velocity components in terms of the two wire voltages. One may also compare the results obtained with an x-wire to results obtained by a single-wire probe for the streamwise velocity component. The agreement between the two sets of data was excellent, providing some validation of x-wire calibration technique.

Finally, the normally operated stationary hot-wire probe cannot recognize flow reversal and it rectifies the voltage output. The calibration technique allows points exceeding the angular limits of the calibration to be readily identified. The fraction of time that the angle between the instantaneous velocity vector and the hot wire exceeded the calibration limits is negligible provided $y/\theta \geqslant 0.25$. This fraction increases rapidly below $y/\theta = 0.25$ but at this level the hot-wire probe remains within the calibration limits 93% of the time. Although it is clear that the region of uncertainty is so thin ($y/\theta < 0.25$) that it is insignificant in the overall momentum budget and scaling considerations, a detailed comparison between data obtained with a single hot wire and an LDV was made. A single wire that was parallel to the surface was chosen for the test because of its small size and its ability to be brought very close to the solid surface. Simultaneous measurements of mean velocity with both instruments validated the data taken earlier with hot wires only (figure 5). There is an excellent agreement between the mean velocity profiles acquired with the LDV and the hot wire even in regions that are very close to the wall. The LDV was able to provide sufficiently accurate, high-resolution data in the linear region next to the surface (figure 5*a*), from which the friction velocity, $u_\tau = \sqrt{\tau_w/\rho}$, could be estimated ($u_\tau^2 = v\partial U/\partial y$). However, the value of u_τ obtained in this way was somewhat higher (by approximately 10%) than the one obtained by using the Clauser method (i.e. the universal, logarithmic law of the wall). Using the friction velocity estimated from figure 5 the short logarithmic relation fitting the data is $u^+ = 5.5 \log y^+ + 2$. The agreement between the hot wire and the LDV data when both are plotted in wall variables (see figure 5*b*) is impressive in view of the anticipated adverse effects resulting from hot-wire rectification. The distributions of the streamwise component of the velocity fluctuations are plotted in figure 5(*c*). The r.m.s. values measured by the LDV system are higher in general, since flow reversal is now taken into account. Surprisingly however, the differences are not large, indicating that the flow reverses relatively rarely. The comparison between the hot-wire data and the LDV was repeated at five different streamwise locations with equally good results.

The surface pressure distribution was obtained by connecting a pressure transducer to surface-pressure taps via a Scannivalve. Pressure taps were placed in three parallel rows along the expansion for additional confirmation of two-dimensionality.

4. Mean flow

The development of the mean flow in the direction of streaming for the two initial conditions (cases A and B) considered, is shown in figure 6. The streamwise distance

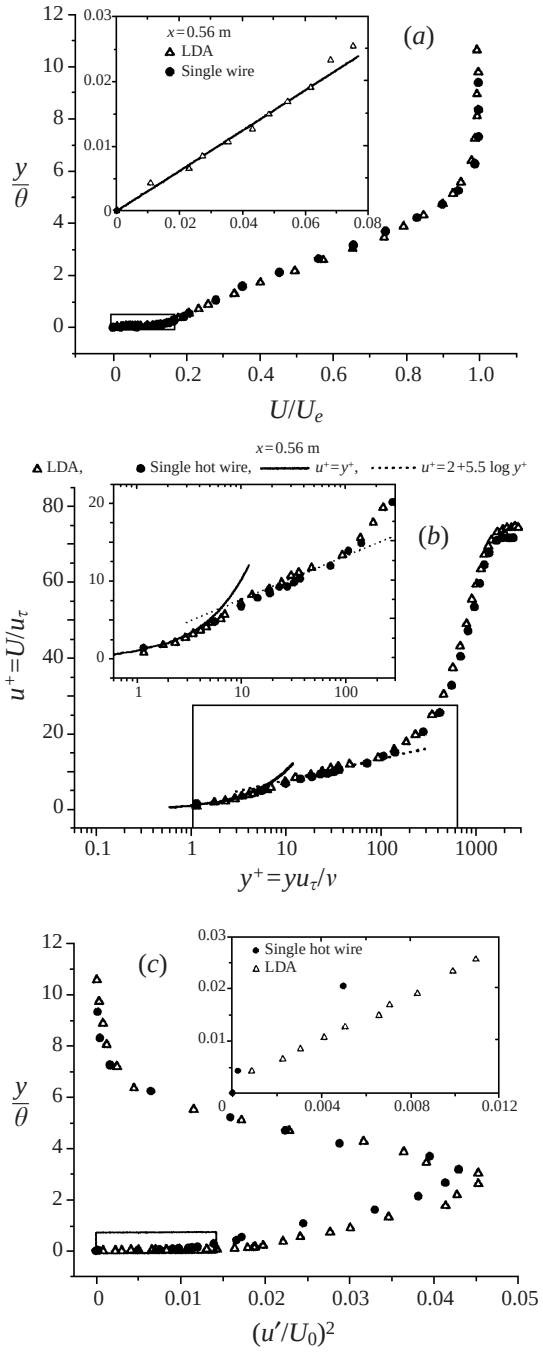

FIGURE 5. Mean and fluctuation velocities measured with the LDV and the hot wire.

is measured from a virtual origin defined by extrapolating the momentum thickness,

$$\theta = \int \frac{U}{U_e}\left(1 - \frac{U}{U_e}\right) \mathrm{d}y,$$

to zero (where U_e is the local free-stream velocity). The reference velocity and length

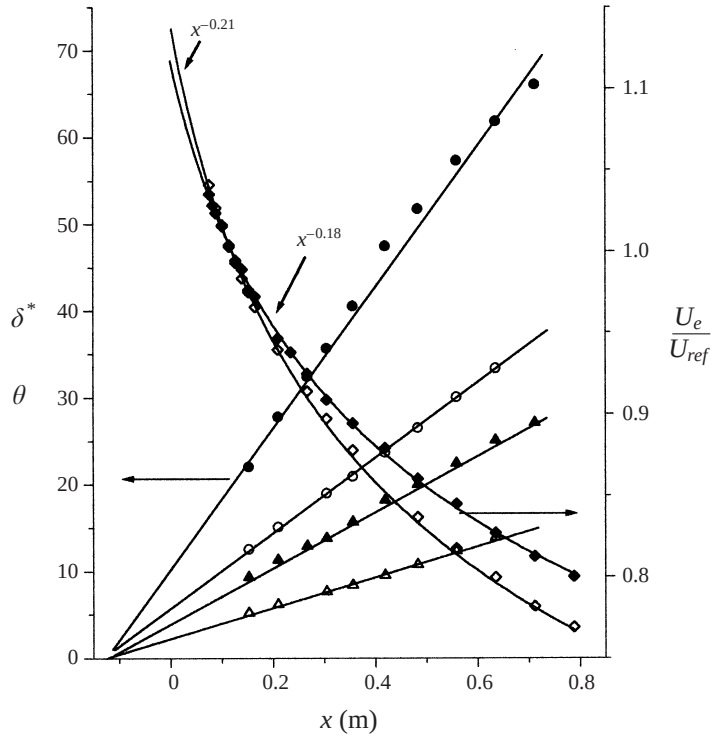

FIGURE 6. Development of the mean flow in the direction of streaming for the two initial conditions (cases A and B): △, ▲θ; ○, ● δ^*; ◇, ◆, U_e/U_{ref}. Open symbols: $\theta_0 = 2.3$ mm, solid symbols; $\theta_0 = 4.5$ mm.

scales used throughout this article are defined as the maximum measured free-stream velocity, U_0, and the extrapolated momentum thickness, θ_0, at the location of the free-stream velocity maximum, respectively. The flow accelerated upstream of the ramp, resulting in values of $U_0 = 17.8\,\mathrm{m\,s^{-1}}$ and $16.7\,\mathrm{m\,s^{-1}}$ with corresponding values of 2.3 mm and 4.5 mm for θ_0, for the two cases A and B considered. This is some 15–20% higher than the $15\,\mathrm{m\,s^{-1}}$ measured by the Pitot tube that was located further upstream in the throat, suggesting that the transition from the flat surface to the ramp was perhaps too rapid when compared to an ideal airfoil design using the Stratford concept. The distance between the location at which the free-stream velocity is maximum and the virtual origin of the flow where $\theta = 0$ (located at $x = -0.133$ m) is denoted by x_0.

The free-stream velocity varies as $(x - x_0)^{-0.21}$ and $(x - x_0)^{-0.18}$ for cases A and B respectively when the streamwise distance is measured from the virtual origin (figure 6). The results presented cover a distance of approximately $200\,\theta_0$. Over that distance the free-stream velocity, U_e, was reduced by 12% from its initial reference velocity value U_0. The data presented by DF span a distance over which the free-stream velocity decelerated by 4% only. The equilibrium region in SK's experiment covered a distance of $\Delta x/\theta_0 = 57$ corresponding to a deceleration $\Delta U_e/U_0 = 6.7\%$.

The flow spreads out linearly with increasing x (e.g. $\mathrm{d}\theta/\mathrm{d}x = $ constant, figure 6). The initial thickness of the boundary layer has, however, an enormous effect on the flow divergence although the difference in the pressure gradient between cases A and B is small. The sensitivity of the flow to the initial boundary layer thickness can be

explained by using the momentum integral equation:

$$\frac{\mathrm{d}\theta}{\mathrm{d}x} + (H+2)\frac{\theta}{U_e}\frac{\mathrm{d}U_e}{\mathrm{d}x} = \frac{c_f}{2}, \tag{4.1}$$

where the experimental data give: $\theta \propto x$ and $U_e \propto x^{-n}$ and the skin friction $c_f \to 0$. The group $(H+2)\theta/U_e\,\mathrm{d}U_e/\mathrm{d}x = \text{constant}$ also represents the rate of spread of this boundary layer. Substituting the measured values for H and n, one gets

$$(\mathrm{d}\theta/\mathrm{d}x)_B = 1.72(\mathrm{d}\theta/\mathrm{d}x)_A.$$

The experimental comparison of the growth rate of θ between cases A and B yielded a slightly larger constant of 1.84 instead of the 1.72 anticipated. We should mention that the virtual origins for both flows were almost identical.†

The sensitivity of this boundary layer to inflow (upstream) conditions sheds some new light on previous observations and explains some of the discrepancies among them. Spangenberg *et al.* (1967) generated two very different boundary layers (the differences were most apparent in the turbulent intensities measured and in their distribution across the flow) by changing the upstream pressure gradient very slightly. DF made similar observations; since they had a fine control over their upstream pressure gradient they could change the sign of c_f by this procedure. In the region in which measurements were presented (i.e. for $x > 1.13\,\mathrm{m}$) the pressure gradient for all three cases they considered was identical. The slight differences in the upstream pressure gradient that they introduced altered the initial thickness of the boundary layers (see figure 3 of DF) and thus changed the character and direction of the entire flow.

The assumption that the initial thickness of such a boundary layer represents the most significant parameter governing its growth enabled us to collapse the rate of spread of the dimensionless (θ/θ_0) of DF, SK and the present two experiments, onto a single curve (figure 7). The displacement thickness, $\delta^* = \int(1 - U/U_e)\mathrm{d}y$, that also spreads out linearly in the direction of streaming, is plotted in figure 6. Its rate of spread is almost twice as large for case B than for case A, nevertheless (δ^*/θ_0) collapses the present experimental results onto those of DF (figure 7). The results of SK are somewhat lower because their flow was not on the verge of separation. Their shape factor, $H = \delta^*/\theta$, was approximately 2 while for the present data H varies slightly with distance and with the case being considered. The assumption of a constant shape factor of 2.45 and 2.55 for case A and B respectively represents most of the data. These values of the shape factor are in close agreement with the observations of Stratford (1959*b*) and have been traditionally used as a criterion for separation.

Mean velocity profiles are presented in figure 8 for cases A and B: but the symbols plotted are for case B only; the mean velocity profiles for case A are represented by the dash-dot line. The mean velocity profiles appear to be approximately self-similar when scaled by the local external velocity, U_e, and the boundary layer momentum thickness. The mean velocity gradient near the wall is small but finite and it is slightly larger for case A (see insert in figure 8) suggesting that the flow in case B is closer to separation. Spangenberg *et al.* (1967) also observed a finite velocity gradient near the surface. When the mean velocity profiles are plotted in wall variables, using

† One of the reviewers brought to our attention the similarity analysis of George & Castillo (1993) and Castillo & George (2000) who used a different similarity analysis and a different length scale. After the preparation of this paper we recast some of our data in those variables in order to provide a more meaningful discussion of those scales in the future. The results are given in the Addendum.

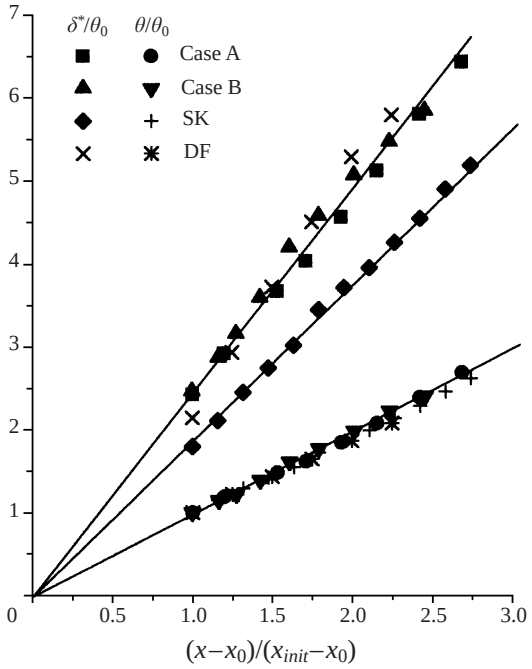

FIGURE 7. Displacement thickness and momentum thickness of the boundary layer versus downstream location for different experimental realizations.

the Clauser method to define a friction velocity u_τ (figure 9*a*), a very large wake component emerges. The value of $u_+ = U/u_\tau$, near the edge of the boundary layer indicates the imminence of the approaching separation. While values ranging from 70 to 80 were observed in case A, they reached 95 for case B data, both numbers comfortably exceeding the values of u_τ obtained by Spangenberg *et al.* (1967). The largest value of u_+ for a zero-pressure-gradient boundary is approximately 25. These results were obtained by assuming, *a priori*, that the inner part of the velocity profiles obeyed the universal law of the wall. In that respect they differ from the velocity profile presented in figure 5(*b*), where u_τ was estimated from the linear part of the law of the wall measured using a LDV.

The entire velocity profile could be adequately represented by Coles' law of the wake, i.e.

$$u_+ = 5.5 + 5.5\log_{10}\left(\frac{yu_\tau}{\nu}\right) + \Pi\sin^2\left(\frac{\pi y}{2\delta}\right). \tag{4.2}$$

Nishri (1996) found that Π is a linear function of $(c_f)^{-1/2}$. The results of the present experiment appear to confirm this conclusion (figure 9*b*). It should be noted, however, that the law of the wake did not match the experimental profile very well at the first measurement station. The variations in the shape factor and the friction coefficient with x are shown in figure 9(*c*). Ideally both H values should be constant when $c_f \to 0$; although they are not, their variation with x is small. It is clear that a decrease in c_f is accompanied by an increase in H. There is a difference in the estimated values of c_f between case A where $c_f = 3.4 \times 10^{-4}$ and B where $c_f = 2.5 \times 10^{-4}$. The very low skin friction described allows one to neglect the right-hand side of the integral momentum equation (4.1). Substitution of the experimental values for H, for θ and for $\mathrm{d}\theta/\mathrm{d}x$ into this equation with $c_f = 0$ implies that $U_e \propto x^{-0.22}$ for case A. This result is in

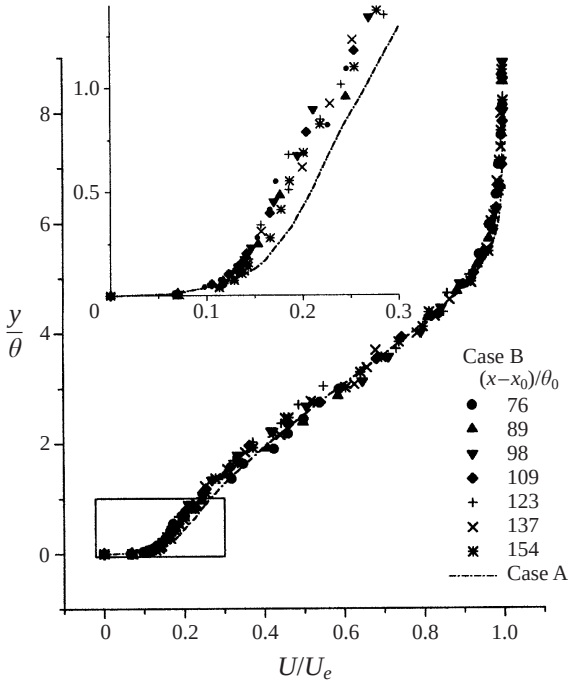

FIGURE 8. Mean velocity profiles for cases A and B.

good agreement with the experimental value, suggesting that the flow is adequately two-dimensional. Further checks on flow two-dimensionality will be described below.

5. Turbulence intensities and scaling

The intensities of the normal and longitudinal components of the turbulent fluctuations are plotted in figure 10(*a*, *b*) using the same length and velocity scales that were used for the mean velocity profile. In contrast to a zero-pressure-gradient boundary layer, there is very little turbulent activity close to the wall; the largest turbulence intensity occurs close to the inflection of the mean velocity profile. The field is highly anisotropic with the longitudinal component of the turbulence intensity for case A being three times greater than the transverse component. The locally normalized turbulence intensity increases with downstream distance and the location of its maximum moves further away from the surface. The Reynolds stresses behave in a similar manner although they seem to increase more moderately with x than $\overline{u'^2}/U_e^2$ does (figure 10*c*). The turbulence, therefore, is not in equilibrium with the mean flow.

Since the mean velocity profile is approximately self-similar, i.e.

$$\frac{U}{U_e} = f'\left(\frac{y}{\theta}\right), \tag{5.1}$$

the scaling of the Reynolds stress and turbulent intensities should be determined by substituting (5.1) into the two-dimensional mean momentum equation

$$U\frac{\partial U}{\partial x} + V\frac{\partial U}{\partial y} + \frac{\partial}{\partial x}\left(\overline{u'^2} - \overline{v'^2}\right) + \frac{\partial}{\partial y}\overline{u'v'} - U_e\frac{\mathrm{d}U_e}{\mathrm{d}x} = 0. \tag{5.2}$$

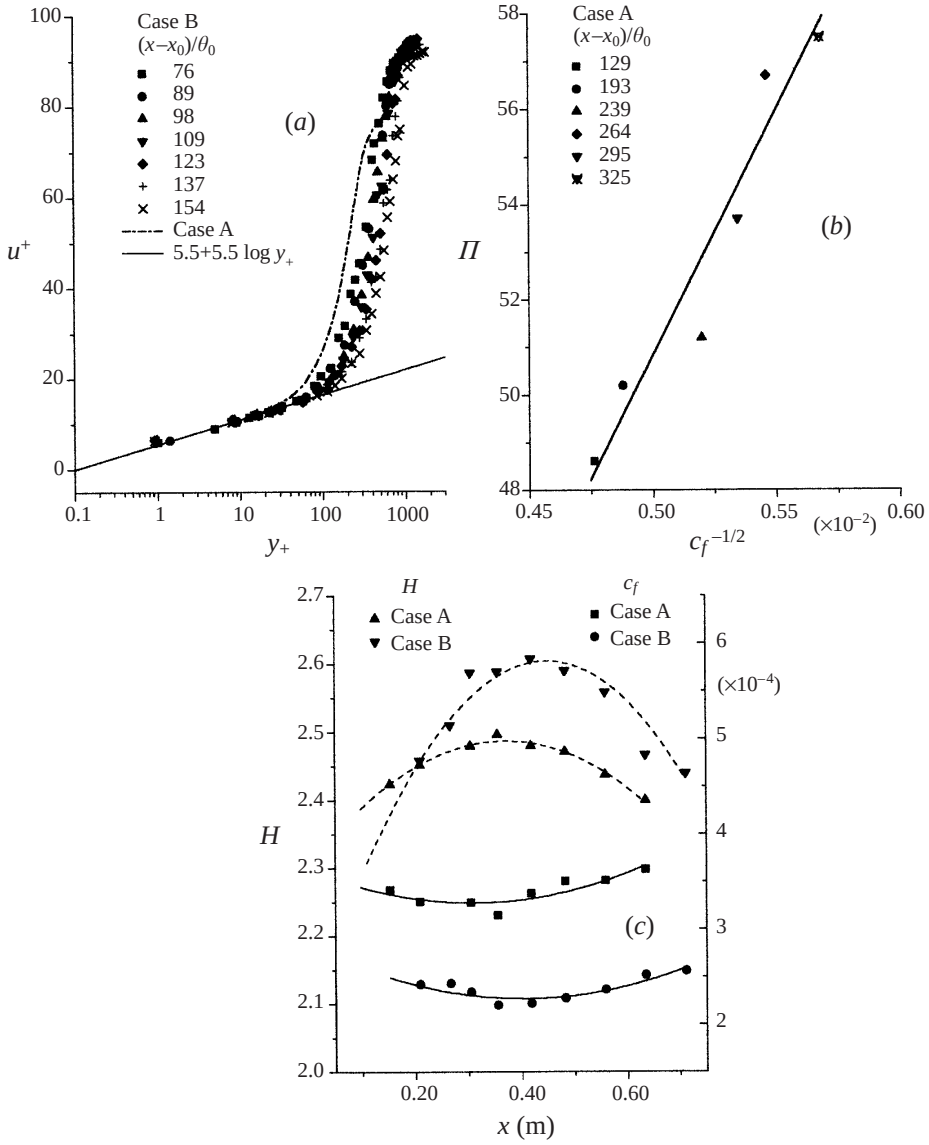

FIGURE 9. (*a*) Mean velocity profiles in wall variables; (*b*) the wake parameter, Π, of the wake law versus the skin friction coefficient; (*c*) variation of the shape factor and the friction coefficient with x.

The equation that results from this substitution is

$$U_e\frac{\mathrm{d}U_e}{\mathrm{d}x}(f'^2 - ff'' - 1) - \frac{U_e^2}{\theta}\frac{\mathrm{d}\theta}{\mathrm{d}x}ff'' + \frac{\partial}{\partial x}\left(\overline{u'^2} - \overline{v'^2}\right) + \frac{\partial}{\partial y}\overline{u'v'} = 0. \tag{5.3}$$

By assuming that the similarity scales can be expressed by power laws of x, i.e. $U_e \propto x^{-n}$ and $\theta \propto x^m$, then

$$U_e\frac{\mathrm{d}U_e}{\mathrm{d}x} \propto \frac{U_e^2}{\theta} \propto x^{-2n-1},$$

implying that, even if similarity of the inertial terms holds true, it does not provide

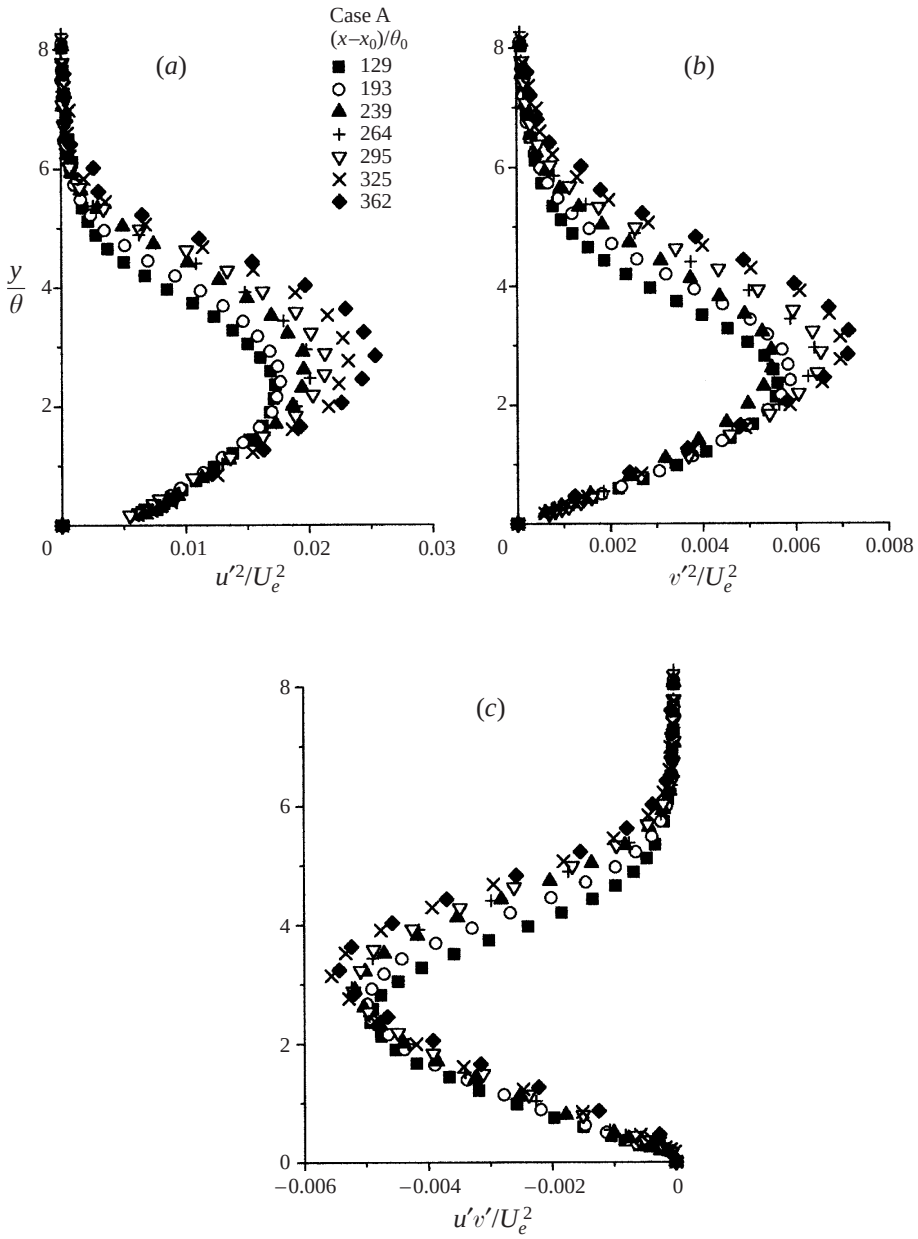

FIGURE 10. Intensities of the normal and longitudinal components of the turbulent fluctuations and the Reynolds stresses normalized with the mean velocity scales.

information about the rate of spread of the momentum thickness m. Experiments clearly indicate that $\theta \propto x$ and therefore $(U_e^2/\theta)\mathrm{d}\theta/\mathrm{d}x$ should vary as $x^{-1.42}$ for case A and as $x^{-1.36}$ for case B. In order to determine m an assumption must be made about the development of the Reynolds stress. The generally accepted choice is

$$\overline{u'v'} = U_e^2 g_{12}(y/\theta) \tag{5.4}$$

because in the traditional self-similar equilibrium flows all turbulent quantities scale

in the same way as the inertial terms (the analysis of Castillo & George is excepted). Examination of the data (figure 10) reveals, however, that this is not appropriate. An alternative representation,

$$\overline{u'^2} = U_0^2 g_{11}(y/\theta), \quad \overline{v'^2} = U_0^2 g_{22}(y/\theta), \quad \overline{u'v'} = U_0^2 g_{12}(y/\theta), \tag{5.5}$$

collapses the maxima of the normal stresses (e.g. $(\overline{u'^2}/U_0^2)_{\max}$) onto a single value that does not occur at a single (y/θ) location; however, it also implies that $m = 2n + 1$, which contradicts the observation that $\theta \propto x$ (i.e. $m = 1$).

The approximate exponent for which the divergence of the maxima in the turbulence intensities away from the surface with increasing x stops was found to be $\theta^{1.2}$, provided only two significant figures were considered. This dependence on θ may be obtained by multiplying the non-dimensional (y/θ) location used for the mean velocity profiles by a local Reynolds number ($Re_\theta = U_e\theta/\nu$), raised to the -0.2 power. Figure 11 demonstrates the improvement in the non-dimensional turbulence profiles when the new length scale is combined with U_0 (a constant velocity) as the velocity scale. The turbulence intensity measured for case B also scaled with the same variables; however, it was 40% higher (figure 11*a*). This implies that identical scaling is applicable to both cases although the proportionality constants may differ depending on the inflow conditions (i.e. $\theta \propto x; \theta_A = C_A x$ and $\theta_B = C_B x$).

For consistency reasons one may assume that the turbulent length scale is also appropriate for scaling the mean velocity profile, i.e.

$$\frac{U}{U_e} = f'\left(\frac{y}{\theta} Re^{-0.2}\right) = f'(cyx^{-k}) \tag{5.6}$$

and substitute (5.6) into the two-dimensional mean momentum equation to give

$$U_e \frac{\mathrm{d}U_e}{\mathrm{d}x}(f'^2 - ff'' - 1) - C\frac{U_e^2}{\theta}\frac{\mathrm{d}\theta}{\mathrm{d}x} ff'' + \frac{\partial}{\partial x}(\overline{u'^2} - \overline{v'^2}) + \frac{\partial}{\partial y}\overline{u'v'} = 0, \tag{5.7}$$

where C is a constant depending on c and k defined in equation (5.6). This equation still scales the inertia terms in the same way as before, however,

$$U_e \frac{\mathrm{d}U_e}{\mathrm{d}x} \propto \frac{U_e^2}{\theta}\frac{\mathrm{d}\theta}{\mathrm{d}x} \propto x^{-1.4} \tag{5.8}$$

and it leads to the requirement that $(\partial/\partial y)(\overline{u'v'}) \propto x^{-1.4}$. The intensity scale that satisfies this requirement is the product of the reference velocity and the local external velocity, $U_0 U_e$ (i.e. $\overline{u'v'} = U_0 U_e g_{12}((y/\theta)Re^{-0.2})$, see figure 11(*d*).

Figure 12 depicts the mean velocity profiles when scaled by the turbulent length scale $L = \theta Re_\theta^{0.2}$. Although the similarity of the inner region is improved, the outer part of the profile shows some deviation from similarity, particularly for case A. The data for case B are displaced and agree quite well with the proposed scaling. In this case the similarity of the outer flow is better. The deviations from self-similarity may be due to the normal stress terms, which are relatively important in the present flow. The intensity scale used for the turbulent fluctuations implies that

$$\frac{\partial}{\partial x}(\overline{u'^2} - \overline{v'^2}) \propto x^{-1}\phi\left(\frac{y}{\theta} Re_\theta^{-0.2}\right), \tag{5.9}$$

and it is not consistent with the development of the inertial terms and the Reynolds stress. The normal stress term (5.9) is often neglected in boundary layer flows because of the boundary layer approximation and the tendency of turbulent flow to isotropy.

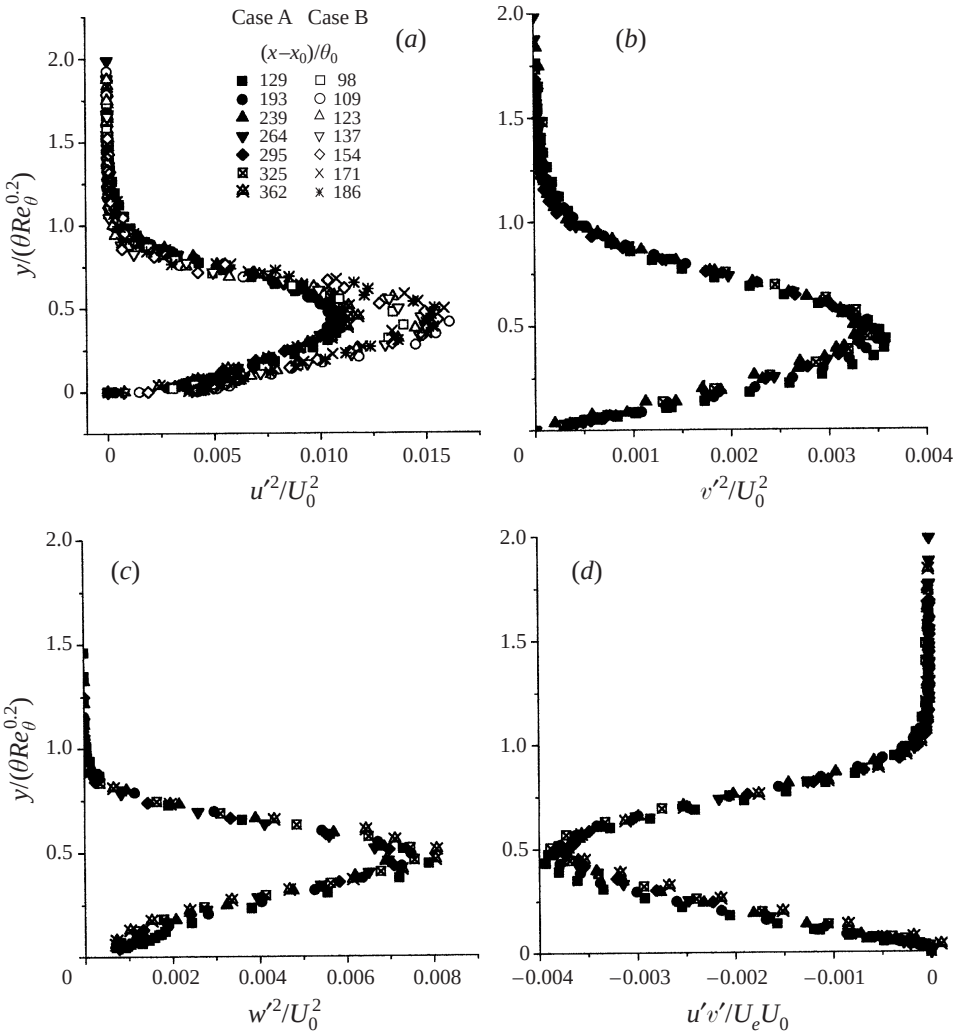

FIGURE 11. Non-dimensional turbulence profiles scaled by the new length scale, $L = \theta Re_\theta^{0.2}$, and a constant velocity U_0.

In this case, however, it contributes as much as 30% to the momentum budget (see figure 2).

The fact that the turbulence intensity, the Reynolds stress and the mean velocity do not share a common velocity scale indicates a lack of local equilibrium between the mean flow and the turbulent motion. Thus the flow is not self-preserving in the sense suggested by Townsend. The present scaling is consistent with the momentum equation and it may be associated with the curvature of the surface. There is also a reorganization among the energy-containing eddies because the simple Reynolds stress correlation $\overline{u'v'}/(\sqrt{\overline{u'^2}}\sqrt{\overline{v'^2}})$ is neither a constant across the flow as it is in absence of pressure gradient (i.e. $\overline{u'v'}/(\sqrt{\overline{u'^2}}\sqrt{\overline{v'^2}}) \approx 0.4$) nor does it remain constant with increasing downstream distance. This is also inconsistent with the assumptions made in simple turbulence models (Bradshaw, Ferriss & Atwell 1967) and implies that the phase relation between the u' and v' fluctuations is constantly changing in

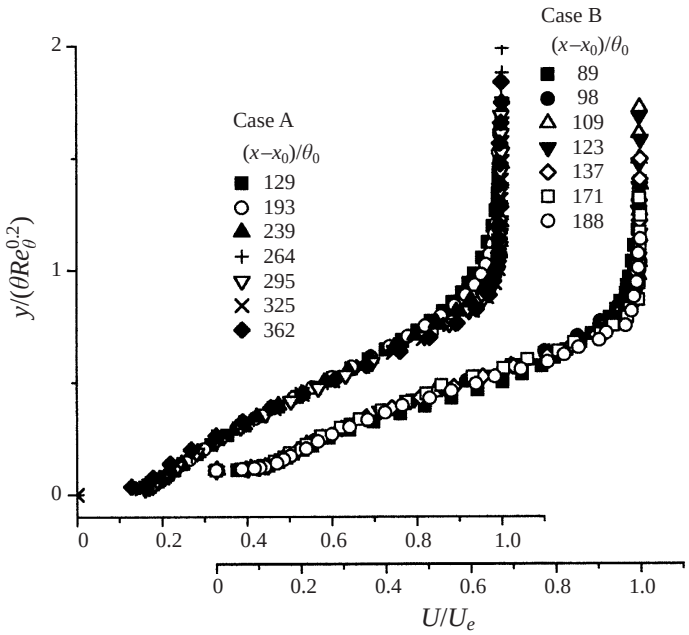

FIGURE 12. Mean velocity profiles scaled by the turbulent length scale L for the thin and the thick upstream boundary layers (cases A and B).

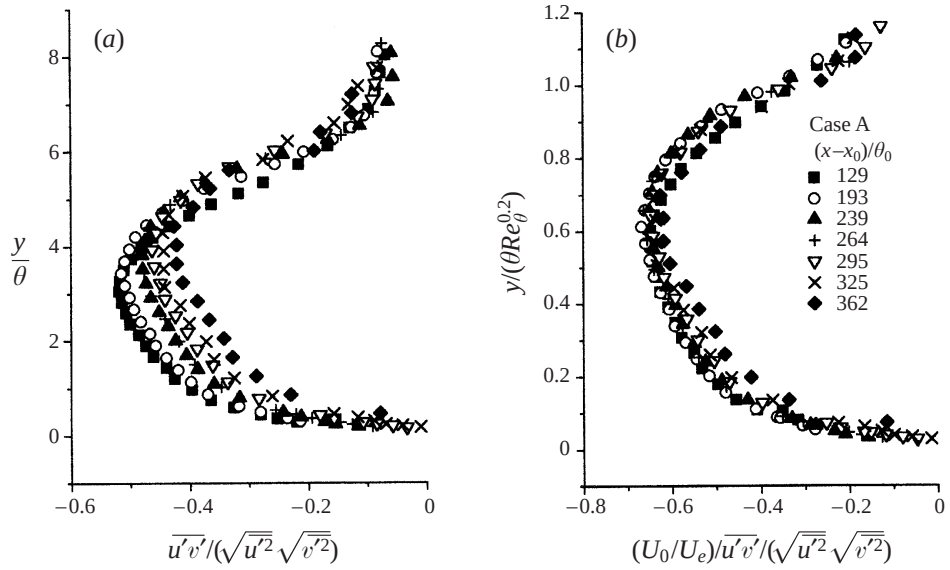

FIGURE 13. Reynolds stress correlation across the flow scaled by: (*a*) the local momentum thickness; (*b*) the turbulent length scale L and re-normalized with the factor U_0/U_e.

this flow. For this reason the quantity $(U_0/U_e)\overline{u'v'}/(\sqrt{\overline{u'^2}}\sqrt{\overline{v'^2}})$ is plotted in figure 13. The similarity of these data is consistent with the above-mentioned scaling and it implies a preferred stretching of the larger and more energetic spanwise eddies.

The skewness factor of the velocity fluctuations is plotted in figure 14 (the subscript 1 corresponds to the streamwise velocity component; 2 corresponds to the normal

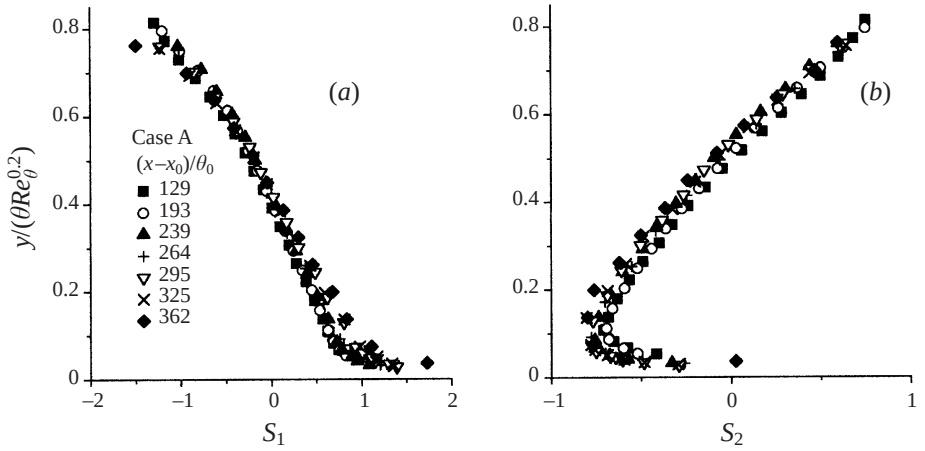

FIGURE 14. Skewness factor of the velocity fluctuations: (*a*) streamwise velocity component; (b) the normal component.

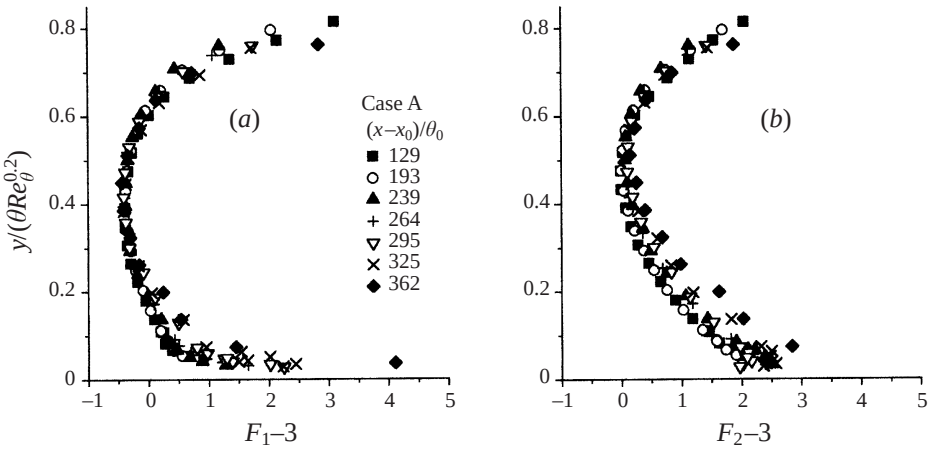

FIGURE 15. Flatness factor of the velocity fluctuations.

component). A non-zero value of this quantity indicates that the probability density function of the fluctuations is non-Gaussian. The skewness profiles exhibit good similarity when the turbulence length scale is used for their normalization; the large increase of the skewness very close to the wall may be partially due to the influence of rectification of the hot-wire sensor. The next higher statistical moment, the flatness factor, is shown as figure 15. A deviation of this value from the Gaussian value of 3 is frequently used as an indicator of intermittency or of the presence of large coherent structures. The reasonable collapse of this quantity when using the turbulence length scale supports the conclusion that the mean coordinate of the laminar–turbulent interface normalized by the local disturbance thickness increases in the streamwise direction. This, in turn, suggests that the scale of the large eddies grows more rapidly than the boundary layer thickness.

The advection speed of the turbulent eddies was measured using the time–space correlation technique at four different downstream locations and at two different normalized y coordinates (figure 16). The results show that eddies of all physical

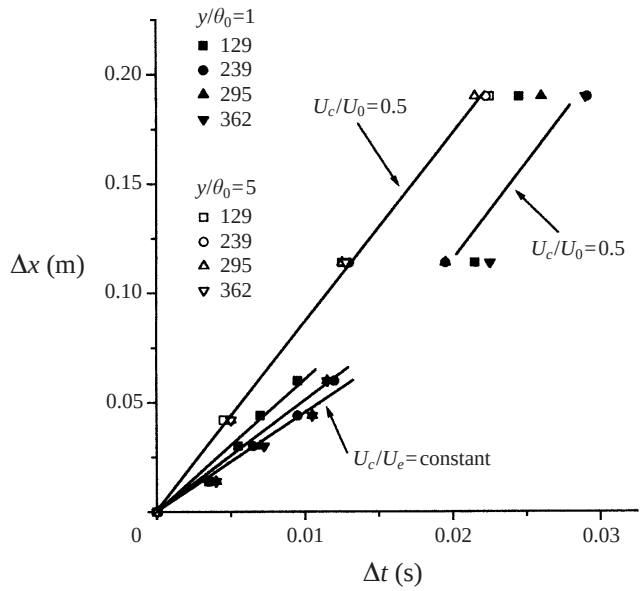

FIGURE 16. Advection speed of the turbulent eddies.

scales propagate at a constant velocity in the outer part of the boundary layer. In the inner layer, physically smaller eddies appear to be advected at a velocity proportional to the local free-stream velocity while larger eddies move at the same constant velocity observed in the outer part of the flow. This suggests that there may be two important scales in the flow; however, to distinguish between them may require instantaneous information along a plane (by using a PIV) rather than two-point information.

6. Turbulent kinetic energy budgets

The energy budgets of the present flow were found to differ radically from what is seen in a zero-pressure-gradient boundary layer, where the turbulence energy is concentrated close to its source of production, the intense shear near the wall. For the present flow the role of the wall appears to be greatly reduced.

The conventional turbulent kinetic energy equation expressed in indicial notation is

$$U_j \frac{\partial}{\partial x_j}\left(\tfrac{1}{2}\overline{u_i u_i}\right) = -\frac{\partial}{\partial x_j}\left(\overline{u_j p} + \tfrac{1}{2}\overline{u_i u_i u_f} - \frac{2}{Re}\overline{u_i S_{if}}\right) - \overline{u_i u_j} S_{if} - \frac{2}{Re}\overline{s_{ij} s_{if}}, \qquad (6.1)$$

where $u_i = U_i + u_i'$, $\quad s_{ij} \equiv \frac{1}{2}\left(\frac{\partial u_i}{\partial x_j} + \frac{\partial u_j}{\partial x_i}\right)$, $\quad S_{ij} \equiv \frac{1}{2}\left(\frac{\partial U_i}{\partial x_j} + \frac{\partial U_j}{\partial x_i}\right)$.

The term on the left-hand side is the rate of transport of turbulent kinetic energy by the mean motion. The first term on the right represents the transport of turbulent energy by pressure fluctuations, velocity fluctuations, and viscous stresses respectively. The viscous term is negligible compared to the remaining terms and was not included in the energy balance. The pressure transport term is not directly measurable; it is obtained from knowledge of the remaining terms. The second term on the right represents the production of turbulence by the interaction of velocity fluctuations and

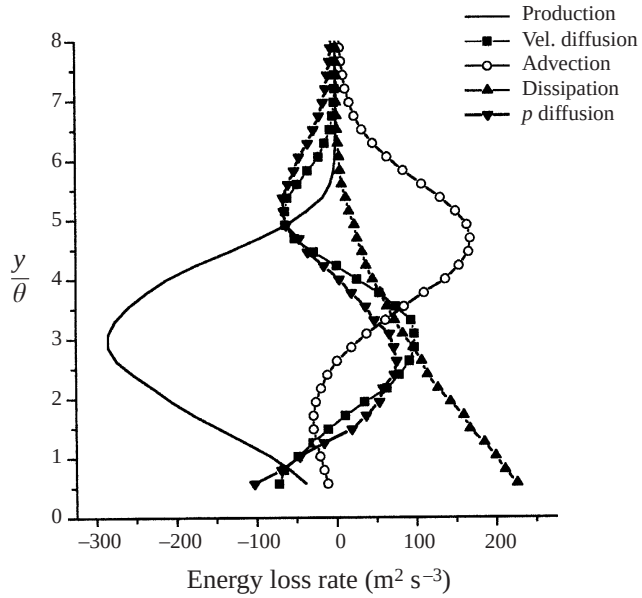

FIGURE 17. Turbulent kinetic energy balance for location $(x - x_0)/\theta_0 = 295$ (case A).

mean strain. The final term on the right-hand side is the dissipation of turbulent energy into thermal energy through the action of viscosity. Several different approximations are used when measuring these terms.

The second term on the right-hand side of equation (6.1) is simplified for a two-dimensional mean flow to

$$\text{Production} = (\overline{u'^2} - \overline{v'^2})\frac{\partial U}{\partial x} + \overline{u'v'}\frac{\partial U}{\partial x}, \tag{6.2}$$

and is dominated by the term involving the Reynolds stress. Production is plotted along with the other terms of equation (6.1) in figure 17 for $(x - x_0)/\theta_0 = 295$. The production of turbulence energy has a strong maximum around $y/\theta = 3$ where both the mean gradient and the velocity correlation $\overline{u'v'}$ have their respective maxima. This is also the location of the inflection in the mean velocity profile as well as the maxima of u' and v'. The correspondence of the inflection point and the production maximum indicates that the flow is dominated by a single inflectional instability, confirming the results of stability theory that show that the peak of the amplitudes of the harmonic oscillations occurs at the same y-location. The hot-wire anemometer is well suited to the exploration of this important region. Because of small uncertainty in the data taken at $y/\theta < 0.25$ (see figure 5) this region was excluded from the energy budget.

The estimation of dissipation requires the use of an approximation because the energy-dissipating eddies are too small to be properly resolved by conventional x-wire probes. Since the turbulence intensity is large, Heskestad's (1965) modification of Taylor's hypothesis was used to obtain the spatial derivative from the measured temporal derivative. This modification replaces the local mean with the instantaneous velocity, i.e.

$$\frac{\partial u_i}{\partial t} = -u\frac{\partial u_i'}{\partial x_j} \tag{6.3}$$

rather than

$$\frac{\partial u_i}{\partial t} = -U\frac{\partial u_i'}{\partial x_j}. \tag{6.4}$$

Heskestad's approximation is considered to be more accurate when large velocity fluctuations are present. The energy-dissipating motions were considered to be isotropic, which allows the turbulent strain rate tensor to be replaced by

$$\text{Dissipation} = 15\overline{\left(\frac{\partial u_1}{\partial x}\right)^2}. \tag{6.5}$$

The dissipation increases monotonically toward the wall, suggesting that a careful exploration of this region is needed in order to understand this process next to the surface. Dissipation seems to be entirely divorced from production and in this respect it resembles the dissipation term in a wake, where the wake centreline corresponds to the surface in the present flow.

For a two-dimensional boundary layer, the convection term becomes

$$\text{Convection} = \frac{1}{2}U\frac{\overline{\partial q'^2}}{\partial x} + \frac{1}{2}V\frac{\overline{\partial q'^2}}{\partial y} \quad \text{where} \quad \overline{q'^2} = \overline{u_i'u_i'}. \tag{6.6}$$

Although the turbulence intensity plotted in non-dimensional coordinates does not vary with downstream distance, the rapid growth of the boundary layer results in a large spatial gradient of q'^2; the first term in equation (6.6) therefore dominates the advection. The peak of advection occurs at about $y/\theta = 4.5$, a relatively small distance inside the boundary layer. In this respect the convection term again resembles the wake rather than the equilibrium boundary layer (see Townsend 1976, pp. 206–207, 293). However, advection is considerably weaker in the inner part of the layer; this contrasts dramatically with the wake, where advection is very strong near the centreline. The advection term is relatively important for the present flow because turbulence produced near the inflection is convected outwards, where dissipation is inadequate to destroy it. This is in contrast to the zero-pressure-gradient case where approximate equilibrium exists between dissipation and production; at present production near the surface is the only term that is dominated by the x-derivative because $\partial u/\partial y$ vanishes. The strong advection may be associated with a more rapid increase in the turbulent length scale relative to the mean length scale.

The diffusion of energy by velocity fluctuations in a two-dimensional boundary layer is given by

$$\text{Diffusion} = \frac{1}{2}\left(\frac{\partial}{\partial y}\overline{v'q'^2} + \frac{\partial}{\partial x}\overline{u'q'^2}\right), \tag{6.7}$$

$$q'^2 = u'^2 + v'^2 + w'^2.$$

The second term is usually negligible in boundary layer type flows; this proved to be the case here. Of the six terms in equation (6.7) four were measured. Previous experiments showed $\overline{w'^2}$ to be approximately twice $\overline{v'^2}$ so $\overline{v'w'^2}$ was taken to be equal to $2\overline{v'^3}$ and $\overline{u'w'^2}$ was taken to be the same as $2\overline{u'v'^2}$. The velocity fluctuations are seen to transport turbulent energy away from its peak (located at about $y/\theta = 3$) toward the surface and toward the edge of the boundary layer. The pressure term is obtained by subtracting the remaining terms on the right-hand side of equation (6.1) from those on the left-hand side. Pressure transport has the same sign and approximately the same magnitude as the velocity transport term in the outer part of the layer. This again is analogous to the wake (see, for example, Hinze 1959), although the

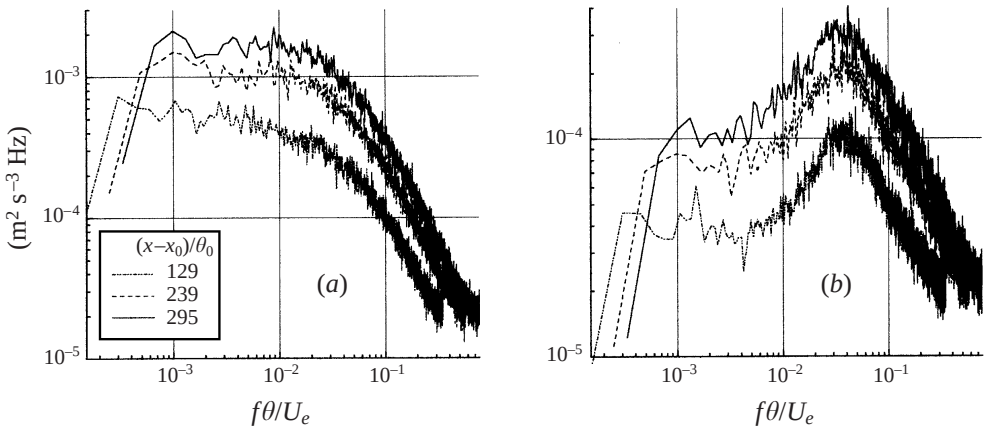

FIGURE 18. Power spectra of the velocity fluctuations at $y/\theta = 5$ for three downstream locations and for: (*a*) u' and (*b*) v' velocity components.

pressure transport term has a greater significance in this flow, particularly as the wall is approached.

In order to identify and determine the scaling parameters of the large coherent structures in the flow, power spectra of the velocity fluctuations were measured (figure 18). In order to reduce the variance of the spectral estimate, the time series of approximately three minutes of length, were divided into 64 equal segments. The power spectrum was then computed for each segment, and the segments were averaged. Only those time records obtained in the outer part of the boundary layer show highly distinctive peaks, and then only for the normal component of the fluctuations, v'. The Strouhal number of this peak, being approximately 0.04, closely matches the Strouhal number observed in the mixing layer. This supports the view that the outer part of the present flow resembles a mixing layer that in the mean is in contact with the surface. Furthermore, since the shear layer is dominated by a single, inflectional instability we expect the same to hold true for the present flow. No peak is apparent in the u'-spectrum at any depth of the boundary layer. The spectra exhibit good overall similarity in terms of the predominant frequencies; the general increase in power with downstream distance shown is a result of the broadening of the non-dimensional fluctuation profiles.

7. The effects of periodic excitation

7.1. *The thin forced boundary layer* (*case A*)

The influence of harmonic excitation on the mean flow for case A is shown in figure 19. The increase in streamwise velocities close to the wall suggests that momentum is transferred from the outside toward the inner region. The shape of the velocity profiles becomes fuller when compared with the unforced case, implying that the flow is no longer on the verge of separation. Although the strongest effect of forcing is observed near the surface, the thickness of the boundary layer was also reduced (figure 20). A comparison between the different frequencies of excitation reveals that the mean flow was most receptive to a forcing at 63 Hz, which corresponds to a dimensionless frequency that is based on inflow conditions of $f\theta_0/U_0 = 0.008$. However, the average local dimensionless frequency in the region of interest (i.e. for $150 < (x - x_o)/\theta_o < 350$) corresponding to the 63 Hz excitation is five times larger

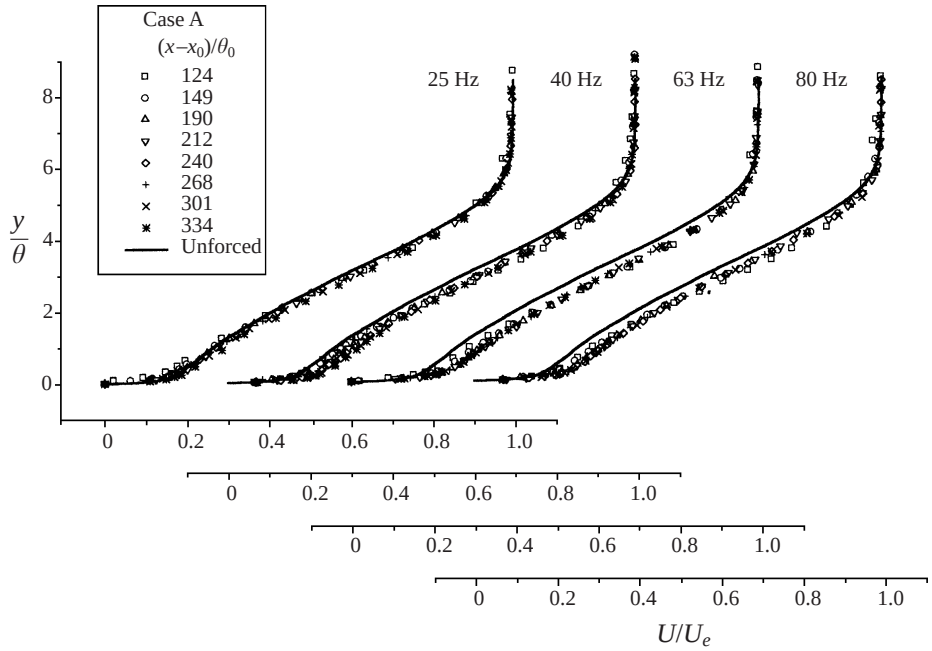

FIGURE 19. The effect of various frequencies of excitation on the mean flow distortion.

(i.e. $f\theta/U_e = 0.04$). For the case of the classical mixing layer between two parallel streams in the absence of pressure gradient this frequency would correspond to the harmonic plane disturbance that had undergone the highest possible amplification by the flow. As can be judged from figure 20, the momentum thickness is not affected by the addition of excitation. This is due to the fact that the most significant change in the mean velocity occurred close to the wall (i.e. in a region in which the velocity is low) and thus the value of the integrand $(U/U_e(1 - U/U_e))$ is insensitive to these changes. On the other hand, the periodic addition of momentum causes a decrease in displacement thickness that is also maximum at $f\theta_0/U_0 = 0.008$ and amounts to 16% of the local δ^*. Thus the boundary layer becomes thinner, and the velocity profile slightly fuller, when high-momentum fluid coming from the outer region is mixed with the fluid in the inner region. The impact of the harmonic excitation on the turbulent intensities may be seen in figure 21. The maximum level of the turbulence intensity was reduced as a result of the excitation at all the forcing frequencies considered; however, the reduction is also highest for the 63 Hz ($f\theta_0/U_0 = 0.008$) excitation. A slightly higher level of fluctuations can be observed close to the wall; however, the accuracy of these hot-wire data is questionable due to possible rectification of the hot-wire response during flow reversals. The observed increase in u' may in fact serve as an indication that the overall duration of the reverse flow periods has diminished due to the excitation because degree of rectification was possibly reduced.

The mean velocity distribution scaled by the friction velocity u_τ with respect to the wall variable $y_+ = yU_\tau v$ is presented in figure 22 for two streamwise locations. It is evident that higher-frequency excitation reduced the maximum value of $(u_+)_{\max} = U_e/u_\tau$ from its initial value of 80 to approximately 65. The linear region of this semi-logarithmic plot was also used to estimate the friction velocity and to calculate the friction coefficient $c_f = 2(u_\tau/U_e)^2$ as well. The impact of harmonic excitation on skin friction is summarized in figure 23(*a*). The lowest excitation frequency had

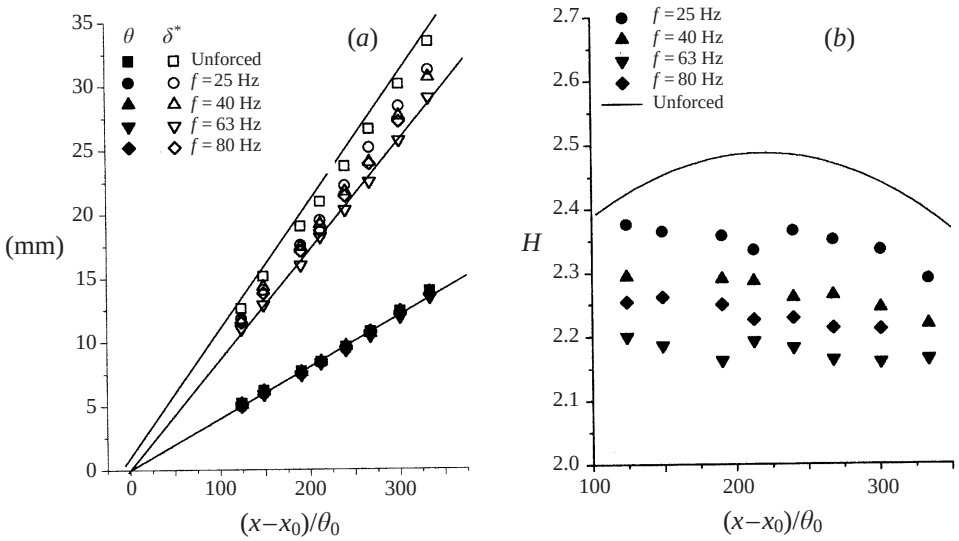

FIGURE 20. The effect of excitation on the integral parameters of the flow.

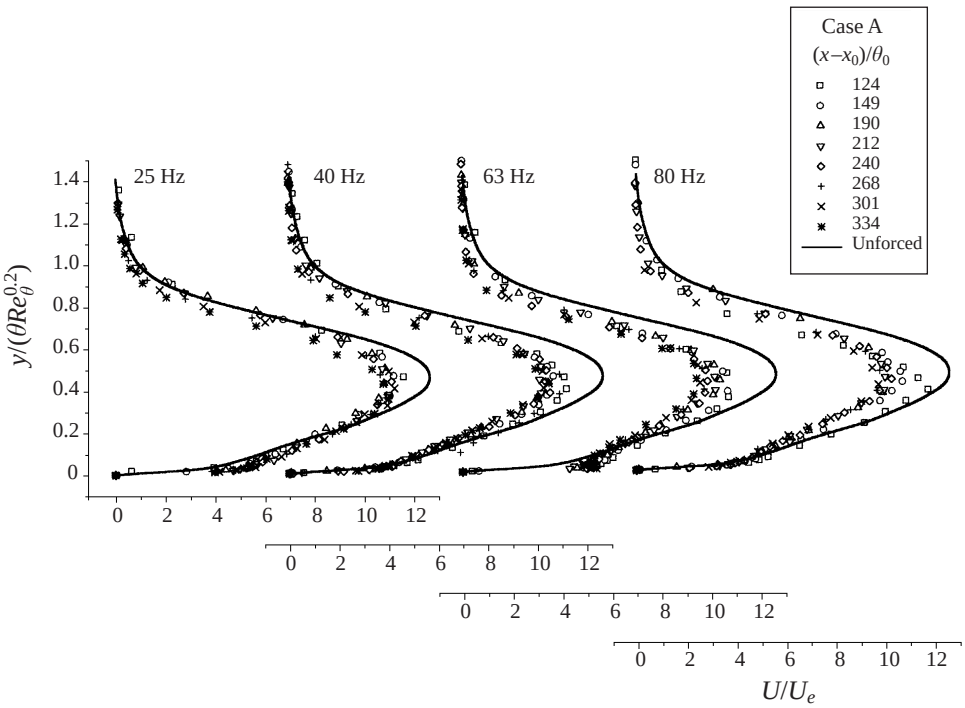

FIGURE 21. The effect of excitation on the turbulence level in the flow.

no effect on c_f for all the x values considered; however, when the frequency was increased to 40 Hz, c_f increased almost monotonically with increasing distance. At the excitation frequency of 63 Hz c_f was essentially constant throughout and was approximately 60% higher than for the unexcited flow. This increase is a direct result of the momentum transferred to the mean flow near the surface by the large eddies.

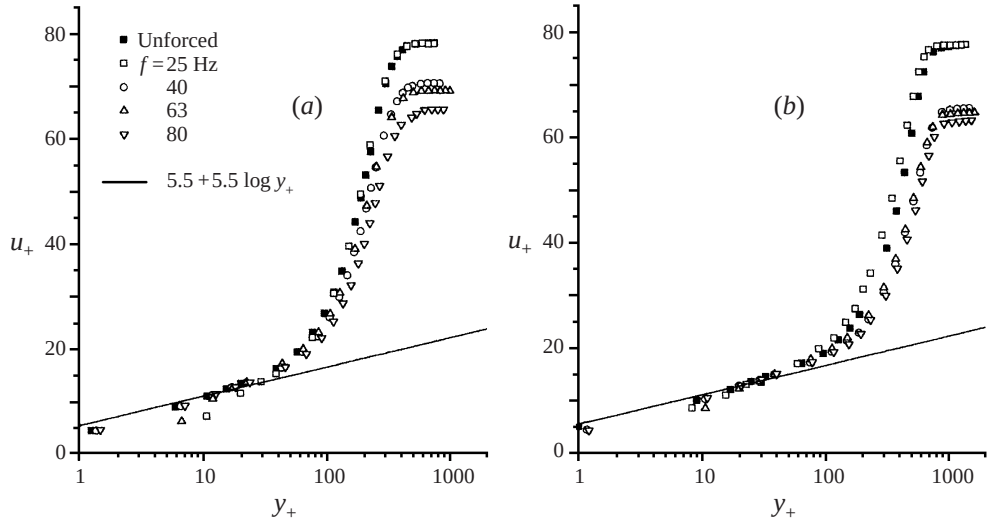

FIGURE 22. The effect of excitation on the wake component in the velocity profile. (*a*) $(x - x_0)/\theta_0 = 124$, (*b*) $(x - x_0)/\theta_0 = 301$.

The average skin friction over the measured interval is plotted in figure 23(*b*) together with the shape factor, H. The latter also decreased due to the excitation.

In order to determine growth and decay of the pertubations introduced the coherent energy was calculated according to

$$\left.\begin{array}{ll} \text{total coherent energy} & \displaystyle\int_0^\infty \langle u'\rangle^2(x,y)\mathrm{d}y \Big/ \int_0^\infty \langle u'\rangle_f^2(x_0,y)\mathrm{d}y, \\ \text{contribution of fundamental} & \displaystyle\int_0^\infty \langle u'\rangle_f^2(x,y)\mathrm{d}y \Big/ \int_0^\infty \langle u'\rangle_f^2(x_0,y)\mathrm{d}y, \\ \text{contribution of 1st harmonic} & \displaystyle\int_0^\infty \langle u'\rangle_{2f}^2(x,y)\mathrm{d}y \Big/ \int_0^\infty \langle u'\rangle_f^2(x_0,y)\mathrm{d}y. \end{array}\right\} \tag{7.1}$$

The results are plotted in figure 24. Surprisingly, the modes that have undergone the highest amplification, like the 25 Hz mode (figure 24*b*), had no significant effect on the mean flow. Decaying modes (like the 63 Hz excitation) on the other hand distorted the mean velocity profile and removed the flow from the brink of separation. It seems that the first harmonic of the forcing frequency (figure 24*c*) plays an important role in distorting the mean flow.

7.2. *The thick forced boundary layer* (*case B*)

In the second test the upstream boundary layer was artificially thickened to $\theta_0 =$ 4.5 mm, through the addition of roughness. The flow was now forced at two different frequencies and two forcing levels. In order to retain dimensionless frequencies $F = f\theta/U_e$ comparable with the former case, the forcing frequencies had to be lowered since the average local momentum thickness was effectively doubled (see figure 6) while the velocity of the free stream remained unaltered. The data presented contain two excitation frequencies: 25 and 40 Hz. The actual forcing level had to be increased as a consequence of the normalization defined in equation (2.1). The results presented correspond to $c_\mu = 0.06\%$ and to $c_\mu = 0.11\%$. The excitation accelerated the flow near the slot, particularly for the higher forcing level. It also generated strong harmonic

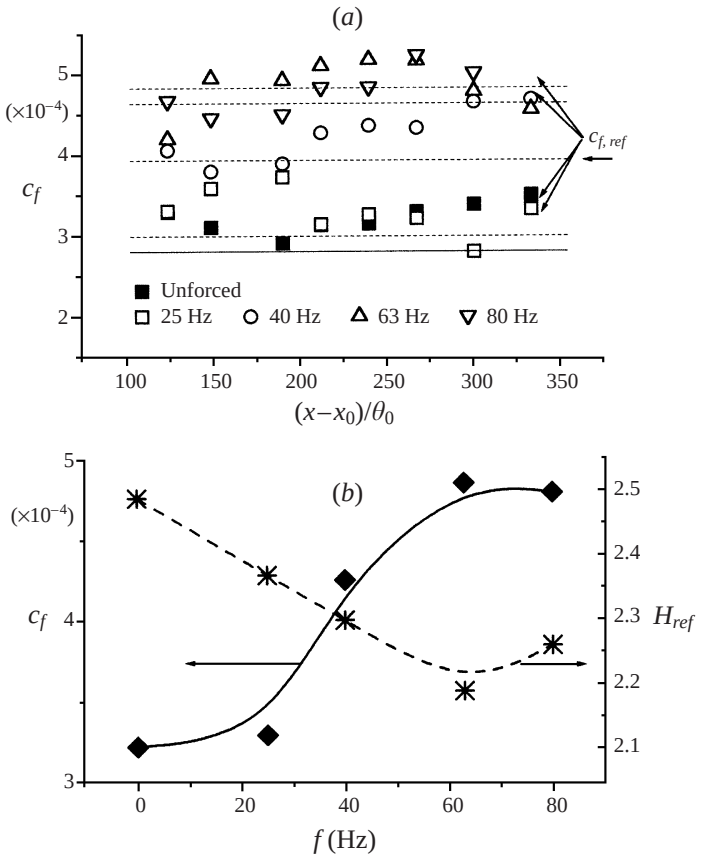

FIGURE 23. The effect of excitation on the skin friction and on H.
The range of integration in (b) is: $(x_2 - x_1)/\theta_0 = 210$.

frequencies at the beginning of the ramp. For the higher c_μ, the first harmonic frequency is even more energetic than the fundamental.

The influence of the harmonic excitation on the shape of the mean velocity profile may be seen in figure 25. The results are similar to the thin, $\theta_0 = 2.3$ mm, inflow conditions. The value of the excited reduced frequencies $f\theta_0/U_0 > 0.008$ distorted the mean velocity near the surface by increasing its value. Now, however, the entire velocity profile appears to be fuller when compared to the results of figure 19. While the increase in the initial, dimensionless forcing frequency from 0.007 to 0.011 does not alter the ensuing mean velocity profile, the forcing level does. A higher forcing level (filled symbols) results in a fuller shape of the mean velocity profile. Both forcing levels remove the flow from the brink of separation.

Figure 26 summarizes the impact of the excitation on the integral length scales of the flow. In contrast to the thin boundary layer experiment, the rate of spread of the momentum thickness, θ, was now decreased slightly by the periodic excitation. This is particularly obvious at larger values of x. The displacement thickness δ^* is affected more by the increase in amplitude than by the change in the frequency, for the two frequencies considered. At the lower amplitude the reduction in $(\mathrm{d}\delta^*/\mathrm{d}x)$ was 12% relative to its unforced value while for the higher amplitudes this reduction reached 20% of its unforced value. As a consequence the shape factor, H (figure 26c), was

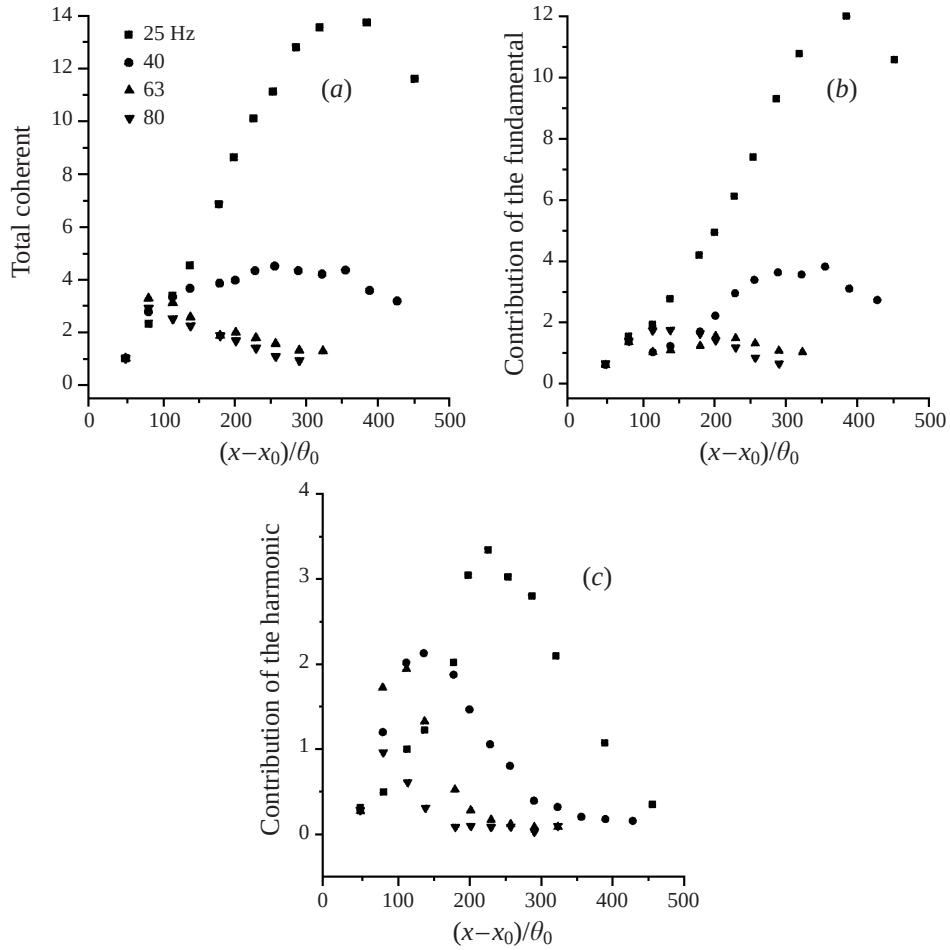

FIGURE 24. The amplification and decay of the imposed perturbations.

reduced from its initial value of 2.5 to 2.35 or 2.1 depending on the amplitude of the excitation. The value of H, however, increases with increasing x while the concomitant value of the friction coefficient (figure 26*b*) decreases with distance. This suggests that the flow will eventually approach the brink of separation (at large values of x) in spite of the level of the plane harmonic excitation that was applied. One may speculate that the effect of decaying perturbations on the mean flow will eventually decrease at larger distances.

The distributions of turbulent fluctuations for the two forcing frequencies and two forcing levels are plotted in figure 27. Plane harmonic perturbations again reduced the level of the turbulent fluctuations and the reduction increased with increasing the input level. If turbulent intensity is a measure of the approaching separation then the reduction of this intensity signifies stabilization of the flow. One may also note that the scaling proposed in § 5 also applies to externally excited flows.

The local amplitudes of the forced perturbations and their harmonics, the amplification factors and the mean velocity field (both with and without the imposed excitation) could provide one with sufficient data to predict the effects of excitation on this flow. It is clear that the mean velocity profile that possesses an inflection

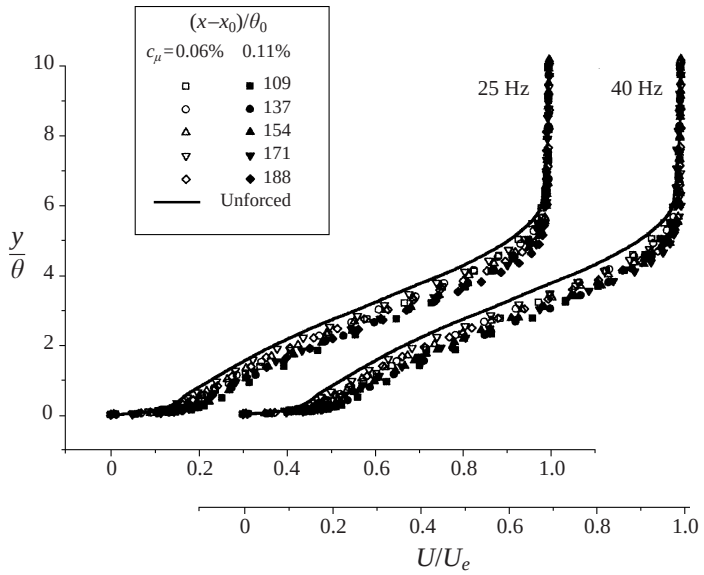

FIGURE 25. The distortion of the mean velocity profiles by periodic excitation of case B.

point is very unstable in the inviscid sense and contributes to the amplification of the imposed perturbations. A classical stability model can thus be used, provided the divergence of the flow is accounted for in the same way as for the mixing layer (e.g. Gaster, Kit & Wygnanski 1985). One may also account for the distortion of the mean flow by considering the leading nonlinear interactions. This was not attempted in the work presented here.

8. Further comparison with previous investigations

Finding a suitable basis for comparison with the results obtained by previous experimenters proved difficult. In the case of Stratford (1959*b*), the region most comparable with the present results (the region of constant shape factor) was specifically noted as being possibly contaminated by secondary flows. It is clear that the developmental history of the two flows is very different. For the experiment reported here the boundary-layer momentum thickness grows by a factor of 6 between the initiation of the adverse pressure gradient and the first experimental profile; in Stratford's case the corresponding ratio is about 2.5. Stratford's initial boundary layer profiles are far from being under conditions of imminent separation, for example the reported shape factor does not exceed 2.0 until the free-stream velocity ratio has fallen to 83% of its initial value. This velocity ratio represents a very substantial pressure rise.

SK claim to have produced an equilibrium boundary layer close to separation; however, their measured shape factor H is 2. In addition, the range of flow development for which they report equilibrium conditions is very short. Over this range the momentum thickness increased by only 42%, whereas for the present flow the ratio of the momentum thickness between the final and the initial stations is 2.52 for case A and exceeds 3 for case B. For an increase in θ that is comparable to SK's even the present measurements would tend to suggest the existence of equilibrium conditions, since only the first two profiles would have been included in the analysis. Closer

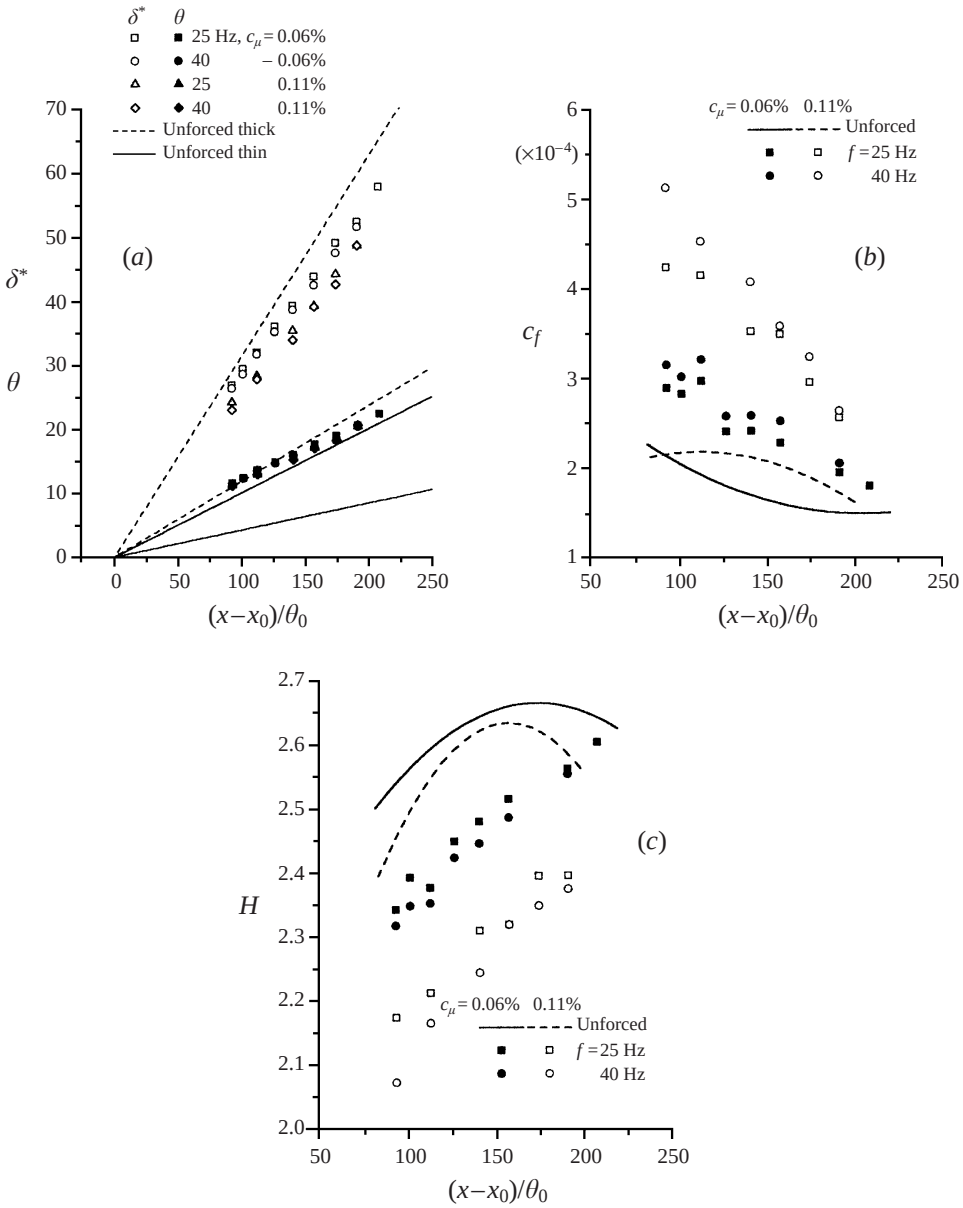

FIGURE 26. The effects of excitation on the integral parameters in case B.

observations of SK's results reveal substantial streamwise development, similar in magnitude to the changes observed over a comparable distance for the present flow.

The experiment most similar to the present investigation, in both instrumentation and procedure, is that of Spangenberg *et al.* (1967). The experimental facility was similar to the one used here but the measurements were done on a flat surface rather than on a curved wall. Provided the comparison is restricted to the region where $(\mathrm{d}\theta/\mathrm{d}x)$ is constant, some results are in reasonable agreement. The exponent they used for the free-stream velocity is, however, much larger (−0.34). The shape factors in this region are comparable (≈ 2.5) but their maximum value of u_+ was somewhat

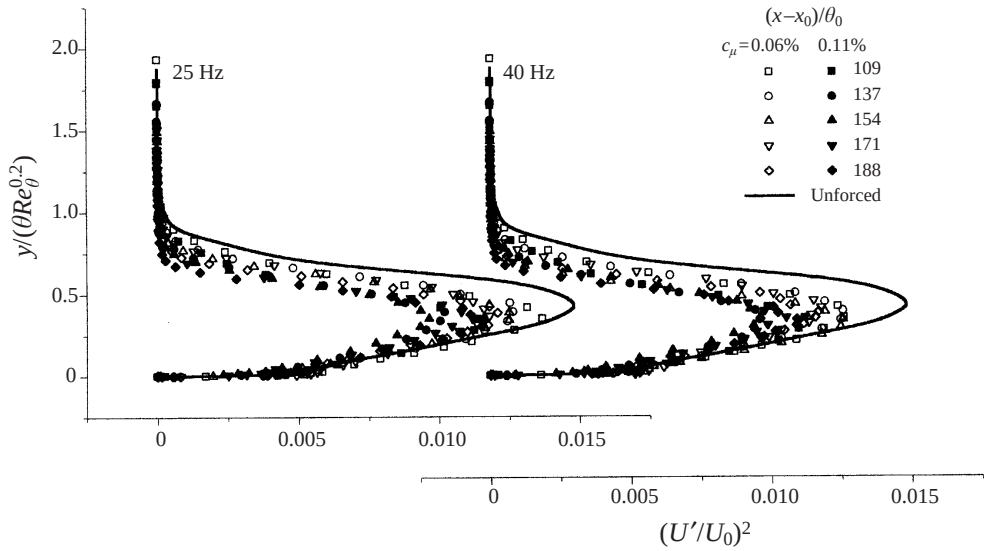

FIGURE 27. The effect of excitation on the turbulence level in case B flow.

	$\frac{u'}{U_0}$	$\frac{v'}{U_0}$
Spangenberg *et al.*	≈ 0.08	≈ 0.055
Present data	≈ 0.10	≈ 0.058

TABLE 1. Comparison of maxima in u' and v'.

lower and it never exceeded 60. The turbulent intensities show the same overall behaviour. In non-dimensional coordinates (in terms of momentum thickness) the location of the maximum intensity moves away from the surface as the flow moves downstream, while the magnitude of the peaks remain approximately constant. The magnitude of the maxima in u' and v' are in reasonable agreement with the present data, as shown in table 1. Significantly perhaps, the Reynolds stress correlation shows the same basic trend as was seen in the present experiment, tending to decrease with downstream distance.

9. Summary and conclusions

Measurements in a boundary layer that was maintained on the verge of separation were made in order to establish its overall statistical behaviour. This boundary layer is extremely sensitive to the upstream flow conditions and its rate of spread is proportional to its initial thickness θ_0. The shape factor of the resulting layer was approximately 2.5, comparable with earlier attempts to produce this kind of flow. Although the flow was driven as close to separation as practicable, the region of zero wall stress predicted by Stratford (1959*a*) was not observed. This is because the smallest increase in the adverse pressure gradient may cause a sudden, total detachment of the flow.

The mean velocity and the turbulence intensity were found to have different

similarity scales, indicative of a lack of equilibrium. Nevertheless the proposed scaling (that is most probably not unique – see George & Castillo 1993; Castillo & George 2000) collapsed the turbulence intensities and the Reynolds stress fairly well and is consistent with the momentum equation. Spectral measurements suggested that the bulk of the flow field was affected by a single, inflectional instability mode. The presence of the solid surface had no influence on the production of turbulence and the convection velocity of the larger eddies. The loss of mean kinetic energy to turbulence production is large in this flow and it may detract from the efficiency of Stratford's concept. Most of the dissipation, however, occurs below the inflection point and attains its maximum close to the surface. The smaller eddies close to the wall are also slower than the larger ones at the edge of the boundary layer and their advection velocity seems to scale with the local free stream. External two-dimensional excitation generated eddies that can be described by an instability of the mean motion (Tumin, Likhachev & Wygnanski 1998). However, only the decaying, smaller eddies increase the skin friction by distorting the mean velocity profile near the surface. This nonlinear process needs to be investigated in the future as it may shed light on the dissipation as well. Finally, the lack of equilibrium might be attributed to surface curvature, which generates streamwise vortices due to centrifugal instability of the mean motion. Such instability is not present when one investigates a flow on the opposing, flat surface. Two-dimensional excitation may, interact and detract from the coherence of the streamwise vortices. This phenomenon is currently under investigation experimentally (P. Nishri & R. Neuendorf, private communication).

This research was supported by the Office of Naval Research, Grant # N00014-94-1, monitored by Dr Patrick Purtell. Thanks are also due to Dr O. Likhachev for his contribution to a better understanding of this experiment.

Addendum

The present experimental results were reprocessed in a manner suggested by George & Castillo (1993), Castillo & George (2000, hereafter referred to as CG) who developed a similarity analysis for turbulent boundary layers in the presence of pressure gradient. The major conclusions are listed below:

A.1. *The pressure gradient parameter* Λ

The similarity of the mean velocity profiles is good in spite of the choice of the boundary layer thickness, δ, to normalize the distance measured from the wall (figure 28*a*). The local Reynolds numbers $Re^* = \delta u^*/\nu$ for case A vary from 450 to 750 and for case B from 700 to 1100. $U_{so}(x)$ in CG's notation is U_e.

The pressure gradient similarity parameter, Λ, may be determined from the slope of either δ, δ^*, or θ when plotted against U_e (figure 28*b*). For case A, the average value of Λ is 0.204; however, $\Lambda = 0.170$ for case B. Coupling CG's definition of Λ with the momentum integral equation,

$$\Lambda = \frac{\delta}{(\mathrm{d}\delta/\mathrm{d}x)} \frac{1}{U_e} \frac{\mathrm{d}U_e}{\mathrm{d}x},$$

$$\frac{\mathrm{d}\theta}{\mathrm{d}x} + (H+2)\frac{\theta}{U_e}\frac{\mathrm{d}U_e}{\mathrm{d}x} = 0.$$

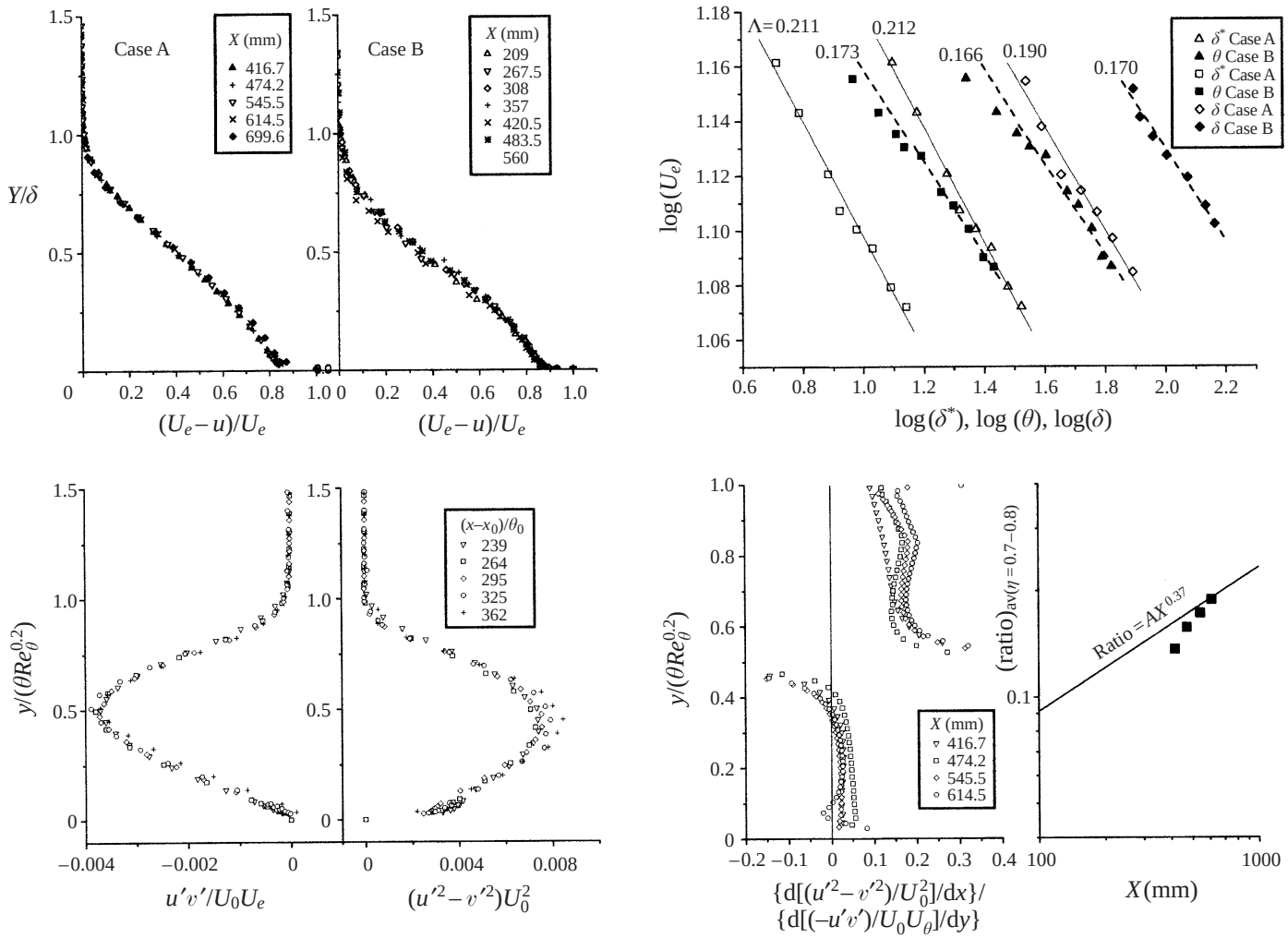

FIGURE 28. The similarity analysis: (*a*) mean velocity profiles, (*b*) pressure gradient similarity parameter, (*c*) Reynolds stress distribution; (*d*) the importance of normal stress.

Assuming $\theta = C_1 X$, $\delta = C_2 X$, the following expression for Λ is derived:

$$\Lambda = \frac{1}{H+2}.$$

For case A where $H = 2.5$, this results in $\Lambda = 0.22$. This is close to the value found using CG's procedure (figure 28*b*). The agreement with case B is less good; perhaps the rate of spread is not perfectly linear or C_f cannot be assumed to vanish.

A.2. *The significance of the normal stresses*

The following discussion is limited to case A only. The normal stress (figures 10 and 11) scale differently from the shear stress (figure 13) and therefore no similarity can be obtained by normalizing these quantities by a single length scale δ. These quantities are replotted in figure 28(*c*) in order to assess the possible significance of the normal stress to the momentum balance. The data collapses by using $(\theta Re_\theta^{0.2})$ as a length scale and two different velocity scales, $U_0 U_e$ for shear stress and U_0^2 for the difference $(u'^2 - v'^2)$.

In order to differentiate the data (to assess the contribution of each term to the momentum budget), the distribution was first smoothed by fitting a Gaussian to the shear stress and a polynomial to the normal stress. The corresponding terms in the momentum equation were calculated and then their ratio was established. The distribution of the ratio between normal stress term and the shear stress term is shown in figure 28(*d*) where a small region near the wall was excluded. Nevertheless the ratio tends to infinity at the inflection point of the mean velocity profile, but otherwise it is approximately constant. It is obvious that the normal stress plays an important role in the outer region (above the inflection point), where it is equal to 20% of the shear stress. Furthermore, this ratio is increasing in the direction of streaming.

By using the scaling laws suggested in the paper one may explore the increasing significance of the normal stress terms in the direction of streaming as follows:

$$\frac{u'^2 - v'^2}{U_0^2} = \Phi(\eta), \quad u'v' = U_0 U_e \Psi(\eta),$$

where $\eta = y/(\theta Re_\theta^{0.2}) = y\nu^{0.2} U_e \theta^{-1.2}$ and $U_e = C_u X^{-0.21}$ and this leads to the expression

$$\frac{\partial}{\partial x}(u'^2 - v'^2) \Big/ \frac{\partial}{\partial x}(-u'v') = C X^{0.37}.$$

By calculating the average ratio for $0.7 < \eta < 0.9$ and plotting it against X the estimated exponent of 0.37 can be observed. Although the accuracy of this procedure is limited, the increasing significance of the normal stresses with X is important. A number exceeding 20% suggests that one cannot neglect the role of the normal stresses in the similarity analysis.

A.3. *A discussion of the suggested equilibrium*

Although the normalized mean velocity profiles collapse fairly well (figure 28*a* and Λ is almost constant in the streamwise direction, the flow is not necessarily in equilibrium. Our measurements indicate that the mean motion, the shear stress and the normal stresses require different scaling. Moreover the significance of the normal stress increases in the direction of streaming. It thus represents typical behaviour of a boundary layer that is not in a state of equilibrium.

REFERENCES

Bradshaw, P., Ferriss, D. H. & Atwell, N. P. 1967 Calculation of boundary layer development using the turbulent energy equation. *J. Fluid Mech.* **28**, 593–616.

Castillo, L. & George, W. K. 2000 Similarity analysis for turbulent boundary layer with pressure gradient: the outer flow. *AIAA Paper* 2000-0913.

Chang, P. K. 1976 *Control of Flow Separation.* Hemisphere.

Dengel, P. & Fernholz, H. H. 1990 An experimental investigation of an incompressible turbulent boundary layer in the vicinity of separation. *J. Fluid Mech.* **212**, 615–636 (referred to herein as DF).

Fernholz, H. H. 1993 Management and control of turbulent shear flows. *Z. Angew. Math. Mech.* **73**, 287–300.

Gad el Hak, M., & Bushnell, D. M. 1991 Separation control: review *Trans. ASME* I: *J. Fluids Engng* **113**, 5–29

Gaster, M., Kit, E. & Wygnanski, I. 1985 Large scale structures in a forced turbulent mixing layer. *J. Fluid Mech.* **150**, 23–39.

George, W. K. & Castillo, L. 1993 Boundary layers with pressure gradient: another look at the equilibrium boundary layer. In *Near Wall Turbulent Flows* (ed. R. M. C. So *et al.*), pp. 901–910. Elsevier.

Heskestad, G. 1965 Hot-wire measurements in a plane turbulent jet. *Trans. ASME* E: *J. Appl. Mech.* **32**, 721–734.

Hinze, J. O. 1959 Turbulence McGraw-Hill.

Lachmann, G. (Ed.) 1961 *Boundary Layer and Flow Control, its Principles and Applications*, vols. I and II. Pergamon.

Liebeck, R. H. 1973 A class of airfoils designed for high lift in incompressible flow. *J. Aircraft* **10**, 610–617.

Lueptow, M., Bruer, K. H. & Haritonidis, J. H. 1988 Computer-aided calibration of x-probes using a look-up table. *Exps. Fluids* **6**, 115–118.

Nishri, P. 1996 On the dominant mechanisms governing active control of separation. PhD thesis, Tel-Aviv University.

Patrick, W. P. 1987 Flowfield measurements in a separated and reattached flat plate turbulent boundary layer. *NASA CR*-4052.

Perry, A. & Schofield, W. H. 1973 Mean velocity and shear stress distributions in turbulent boundary layers. *Phys. Fluids.* **16**, 2068–2074.

Simpson, R. L. 1989 Turbulent boundary-layer separation. *Ann. Rev. Fluid Mech.* **21**, 205–234.

Skare, P. E. & Krogstad, P. A. 1994 A turbulent equilibrium boundary layer near separation. *J. Fluid Mech.* **272**, 318–348 (referred to herein as SK).

Spangenberg, W. G., Rowland, W. R. & Mease, N. E. 1967 Measurements in a turbulent boundary layer maintained in a nearly separating condition. In *Fluid Mechanics of Internal Flow* (ed. G. Sovran), pp. 110–151. Elsevier.

Stratford, B. S. 1959*a* The prediction of separation of the turbulent boundary layer. *J. Fluid Mech.* **5**, 1–16.

Stratford, B. S. 1959*b* An experimental flow with zero skin friction throughout its region of pressure rise. *J. Fluid Mech.* **5**, 17–35.

Townsend, A. A. 1976 *The Structure of Turbulent Shear Flow*, 2nd Edn. Cambridge University Press.

Tumin, A., Likhachev, O. & Wygnanski, I. 1998 On harmonic perturbations in turbulent shear flows. *Bull. APS* **43**, 2079.

Wygnanski, I. 1997 Boundary layer and flow control by periodic addition of momentum. *AIAA Paper* 97-2117.